



# Brucite-driven CO<sub>2</sub> uptake in serpentinized dunites (Ligurian Ophiolites, Montecastelli, Tuscany)



Chiara Boschi<sup>a,\*</sup>, Andrea Dini<sup>a</sup>, Ilaria Baneschi<sup>a</sup>, Federica Bedini<sup>a,b</sup>, Natale Perchiazzi<sup>b</sup>, Andrea Cavallo<sup>c</sup>

<sup>a</sup> Istituto di Geoscienze e Georisorse, CNR Pisa, Italy

<sup>b</sup> Dipartimento di scienze della Terra, Univ. Pisa, Pisa, Italy

<sup>c</sup> Istituto Nazionale di Geofisica e Vulcanologia INGV, Roma, Italy

## ARTICLE INFO

### Article history:

Received 4 October 2016

Accepted 1 July 2017

Available online 13 July 2017

### Keywords:

Serpentinite

Carbonation

Brucite

Hydromagnesite

Layered double hydroxides

Tuscany

## ABSTRACT

Understanding the mechanism of serpentinite weathering at low temperature – that involves carbonate formation – has become increasingly important because it represents an analog study for a cost-efficient carbon disposal strategy (i.e. carbon mineralization technology or mineral Carbon dioxide Capture and Storage, CCS). At Montecastelli (Tuscany, Italy), on-going spontaneous mineral CO<sub>2</sub> sequestration is enhanced by brucite-rich serpentinized dunites. The dunites are embedded in brucite-free serpentinized harzburgites that belong to the ophiolitic Ligurian Units (Northern Apennine thrust-fold belt). Two main serpentinization events produced two distinct mineral assemblages in the reactive dunite bodies. The first assemblage consists of low-T pseudomorph, mesh-textured serpentine, Fe-rich brucite (up to 20 mol.% Fe(OH)<sub>2</sub>) and minor magnetite. This was overprinted by a non-pseudomorph, relatively high-T assemblage consisting of serpentine, Fe-poor brucite (ca. 4 mol.% Fe(OH)<sub>2</sub>) and abundant magnetite. The harzburgite host rock developed a brucite-free paragenesis made of serpentine and magnetite.

Present-day interaction of serpentinized dunites with slightly acidic and oxidizing meteoric water, enhances brucite dissolution and leads to precipitation of both Mg-Fe layered double hydroxides (coalingite-pyroaurite, LDHs) and hydrous Mg carbonates (hydromagnesite and nesquehonite). In contrast, the brucite-free serpentinized harzburgites are not affected by the carbonation process.

In the serpentinized dunites, different carbonate minerals form depending on brucite composition (Fe-rich vs Fe-poor). Reactions in serpentinized dunites containing Fe-rich brucite produce a carbonate assemblage dominated by LDHs and minor amount of hydromagnesite. Serpentinized dunites with a Fe-poor brucite assemblage contain large amounts of hydromagnesite and minor LDHs. Efficiency of CO<sub>2</sub> mineral sequestration is different in the two cases owing to the distinct carbon content of LDHs (ca. 1.5 wt.%) and hydromagnesite (ca. 10 wt.%). Here, for the first time, we link the mineral composition of serpentinized ultramafic rocks to carbonate formation, concluding that Fe-poor brucite maximizes the mineral CCS efficiency.

© 2017 Elsevier B.V. All rights reserved.

## 1. Introduction

Mineral carbonation is a natural analogue of induced mineral Carbon dioxide Capture and Storage (CCS). It is a chemical process that involves the reaction of CO<sub>2</sub>-bearing fluids with silicate minerals (serpentine, olivine) and oxides (brucite) to form carbonate minerals (magnesite, calcite, hydromagnesite, nesquehonite). Mineral CCS is of particular interest to scientists and the industry because of its potential for storing large amounts of anthropogenic CO<sub>2</sub>, during the transition period from fossil fuels to alternative green energy (IPCC, 2005, 2014).

One approach of mineral CCS currently under investigation is ex-situ low temperature mineral carbonation in serpentinites. The development of a complete and viable induced process has been attempted

through laboratory experiments, numerical modelling, and geochemical studies of serpentinites mine tailings and mine shafts (Assima et al., 2013, 2014; Bea et al., 2012; Beinlich and Austrheim, 2012; Bedini, 2016; Boschi et al., 2013a; Gautier et al., 2014; Hänchen et al., 2008; Harrison et al., 2013, 2015; Hövelmann et al., 2012; Loring et al., 2012; Oskierski et al., 2013; Pronost et al., 2011; Wilson et al., 2006, 2009, 2011, 2014; Zarandi et al., 2016; Zhao et al., 2010). It has been demonstrated that the carbonation of serpentinite mine tailings and shafts, at low temperature, sequesters significant amounts of CO<sub>2</sub>, via the formation of hydrous Mg-carbonates ± Layered Double Hydroxides (LDHs). The presence of brucite in serpentinites plays a key role in this process, improving the CCS efficiency (Assima et al., 2013, 2014). Though, brucite is seldom found in oceanic and ophiolitic serpentinites (Bach et al., 2004, 2006; D'Antonio and Kristensen, 2004; Frost and Beard, 2007; Frost et al., 2013; Godard et al., 2008; Hostetler et al., 1966; Klein et al., 2009, 2014; Langone et al., 2013; Mumpton and Thompson, 1966;

\* Corresponding author.

E-mail address: [c.boschi@igg.cnr.it](mailto:c.boschi@igg.cnr.it) (C. Boschi).

Schwarzenbach et al., 2016), despite its formation during the first stages of serpentinization as predicted by theoretical models (Hostetler et al., 1966). A lack of brucite in natural rocks can be attributed to multiple factors: (i) the increase of silica activity during serpentinization that leads to brucite dissolution by the fluid (and magnetite precipitation); (ii) a reduced stability of brucite during high temperature serpentinization; (iii) a tendency of brucite to dissolve in seawater (Jöns et al., 2017) or in low temperature meteoric fluids (forming hydrous carbonates, as already noticed by Hostetler et al., 1966 and Mumpton and Thompson, 1966); (iv) a systematic lower modal estimate of this mineral, being difficult to identify by classical optical microscope.

Here, we investigate the relationship between brucite occurrences in serpentinites and the degree and the type of carbonation, by sampling adjacent carbonated and non-carbonated serpentinite outcrops from Tuscany (Italy).

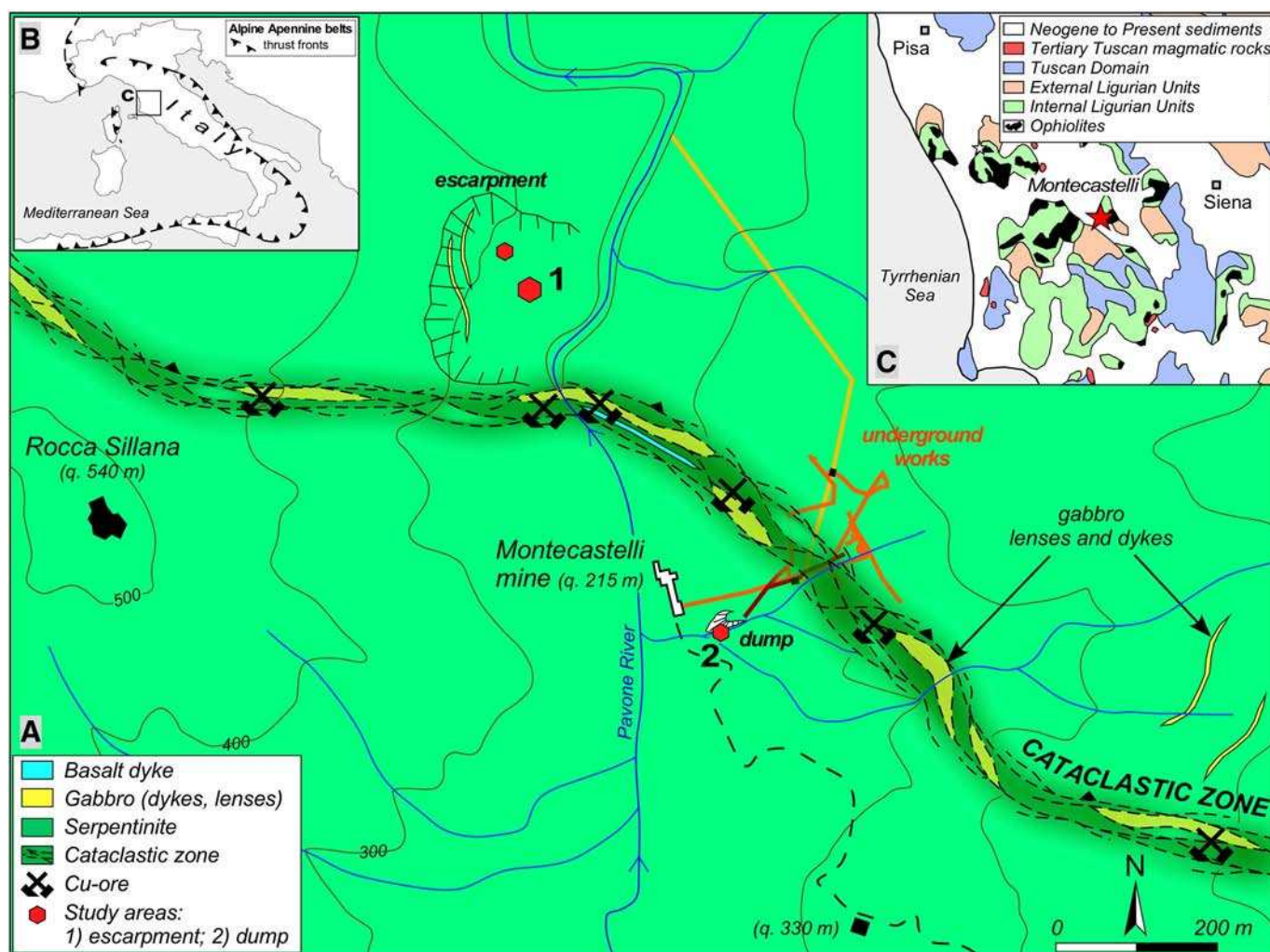
Serpentinites are widespread in Tuscany, but naturally carbonated outcrops only occur in a few areas (Fig. 1; Boschi et al., 2009, 2013b; Langone et al., 2013). At Montecastelli (Southern Tuscany, Fig. 1), pervasive on-going carbonation affects brucite-rich serpentinitized dunite bodies, whereas the hosting brucite-free serpentinitized harzburgites appear mostly unaltered. The mineralogical characterization and petrological observation of the serpentinitized rock types – with particular attention to brucite – and of the associated, newly formed carbonates, allow us to constrain and to quantify the process of carbonation. We show that carbonate formation depends on the different rock mineralogies and on the chemical composition of the involved minerals.

Our results emphasize the role of brucite composition in triggering the formation of distinct carbonate assemblages through a process of sequential development during progressive infiltration/reaction of/with meteoric water.

## 2. Geological background

Tuscany, same as Liguria (Italy) and Corsica (France), is characterized by numerous ophiolites belonging to the uppermost tectonic unit of the Northern Apennine (i.e., Ligurides; Fig. 1). The Ligurides are subdivided in Internal and External Units. The Internal Ligurian Units are characterized by an ophiolitic basement (serpentinized peridotites, gabbros and basalts) and by a Late Jurassic–Early Cretaceous sedimentary cover (radiolarites, limestones and shales). The External Ligurian Units consist of calcareous-marly turbidites (Cretaceous–Palaeocene), containing ophiolite olistoliths and ophiolite-derived debris (Elter, 1975; Marroni and Pandolfi, 1996).

In Southern Tuscany, the Ligurian Units occur in a complex stacking of tectonic sub-units of both Internal and External derivation, including ophiolites, sedimentary cover, and turbiditic sediments. The main ophiolitic bodies, dominated by serpentinites (with minor gabbros and basalts), belong to the Internal Ligurian Units and form an ENE trending, discontinuous alignment (Fig. 1; Nirta et al., 2005 and references therein). This heterogeneous old oceanic basement, typical for slow- and ultra slow-spreading ridges, contains areas with re-worked Cu–Fe ores. The Cu–Fe ores are made up of sulphide nodules, hosted in a soapy and





sheared assemblage of chlorite, Ca-rich amphibole and serpentine, that resembles Cu–Fe VMS oceanic deposits (Bertolani and Rivalenti, 1973; Boschi and Dini, 2015).

Available petrologic-geochemical data on Tuscan serpentinized peridotites are limited (Boschi et al., 2009; Hébert et al., 1989; Langone et al., 2013; Mellini et al., 2005; Serri et al., 1985; Tribuzio et al., 2004), with only few detailed mineralogical and nano-structural studies (Rumori et al., 2004; Viti et al., 2005).

### 3. The Montecastelli ophiolite: field observations

The study area is located near the medieval village of Montecastelli (Southern Tuscany), at the periphery of the Larderello–Travale geothermal area (Fig. 1; Dini et al., 2005). Here, the Pavone River deeply eroded a pluri-kilometric serpentinite body embedded in shales that are up to 300 m in height, resulting in a hilly landscape.

The Montecastelli serpentinites show a dark-green massive and mostly isotropic texture and are crosscut by a pervasive network of randomly oriented chrysotile veins (Fig. 2). The veins, made of grassy green fibrous chrysotile, are of variable thickness (from less than 1 mm to 5 cm) and length (from a few cm to several m). During the deformation, associated with the formation of the Apennine belt, the massive veined oceanic serpentinites have been affected by pervasive fracturing. Structural data indicate that the Apennine-related fracture network does not show a systematic orientation, and mostly exploited pre-existing discontinuities, with re-opening of old oceanic chrysotile veins. Fractures have highly variable areal density (from 1 up to 40 m<sup>-1</sup>), persistence (mm to tens of m) and width (μm to cm). In some cases, serpentinites that are apparently massive can be easily disrupted due to a network of latent fractures. However, connectivity is limited due to the significant

amount of very fine-grained serpentine mud accumulating along fractures, especially at the fracture intersections.

Two main types of serpentinites are recognized: widespread serpentinized harzburgites (here defined as Type 1) embedding metric to decametric bodies of serpentinized dunite (Type 2; Figs. 2 and 3). Macroscopically, the serpentinized dunites differ from the serpentinized harzburgites in the absence/scarcity of bastite/px porphyroclasts and in the ubiquitous occurrence of late serpentine–magnetite–brucite veins. At the periphery of this area, large outcrops of gabbro and basalt are in contact with the sedimentary cover (Serri et al., 1985). Gabbros and locally basalts also crop out in a narrow (ca. 100 m wide, Figs. 1 and 2), NW–SE trending and NE dipping belt that runs across the serpentinites, extending for about 2 km from the eastern to the western sides of the Montecastelli ophiolite outcrop (Lotti, 1885). A cataclastic zone roughly matches the orientation of the gabbro–basalt belt; it is characterized by a soapy assemblage made of chlorite, Ca-rich amphibole, Fe-rich serpentine, andradite and xonotlite, depending on the rock type involved (serpentinites, gabbros or basalts). All along this cataclastic structure, several small re-worked Cu–Fe ores were identified and partially exploited in the past (Fig. 1; Federici, 1941; Lotti, 1885, 1924).

In 1873, D'Achiardi observed and reported for the first time the carbonation of the Montecastelli serpentinite outcrops. Later – after 1970 – this locality has been actively frequented by local mineral collectors for the nice findings of aragonite (prismatic crystals up to 20 cm) and hydromagnesite (crusts of fibrous radiating spherules up to 1 cm) in the carbonated serpentinites.

The intense carbonation here is mostly confined to metric to decametric volumes of serpentinized dunites (Type 2; Figs. 3 and 4). Two of these areas have been selected for this study (Figs. 1 and 4): 1) a large steep escarpment located on the western side of the Pavone River and

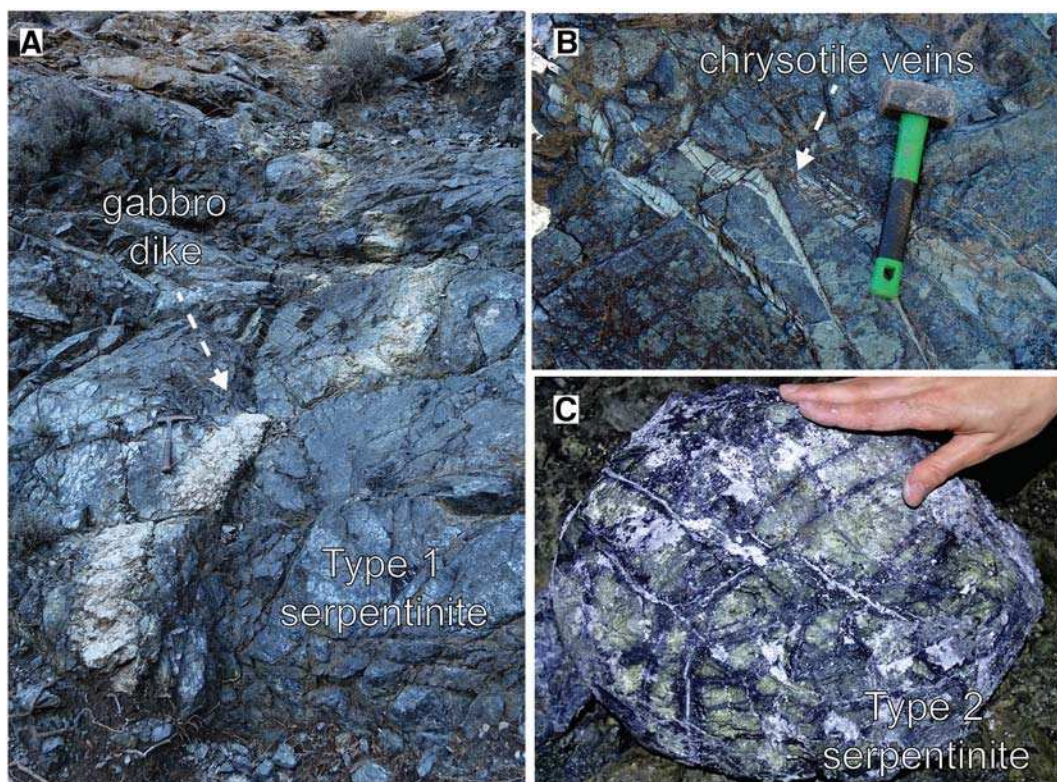


**Fig. 2.** Photos of the Montecastelli outcrops showing the different rock types: A) A dike of gabbro crosscutting massive serpentinized harzburgite (Type 1); B) chrysotile veins in serpentinized harzburgite; C) Serpentinized dunite showing the network of serpentine + Fe-poor brucite + magnetite veins (Type 2b) embedding relics of the mesh textured rock Type 2a. Due to the pervasive dissemination of magnetite, the veins are black. They produce a marked colour contrast with the greenish-yellowish domains that they wrap around. In Tuscany, this serpentinite variety was called “Ranocchiaia” (from Italian language “rana” = frog for the similarity to frog skin) and largely used since Renaissance time as a decorative stone in buildings and for the production and workmanship of semiprecious stone furnishings. Note the preferential precipitation of whitish hydromagnesite in correspondence with the vein network containing Fe-poor brucite (see text for details).



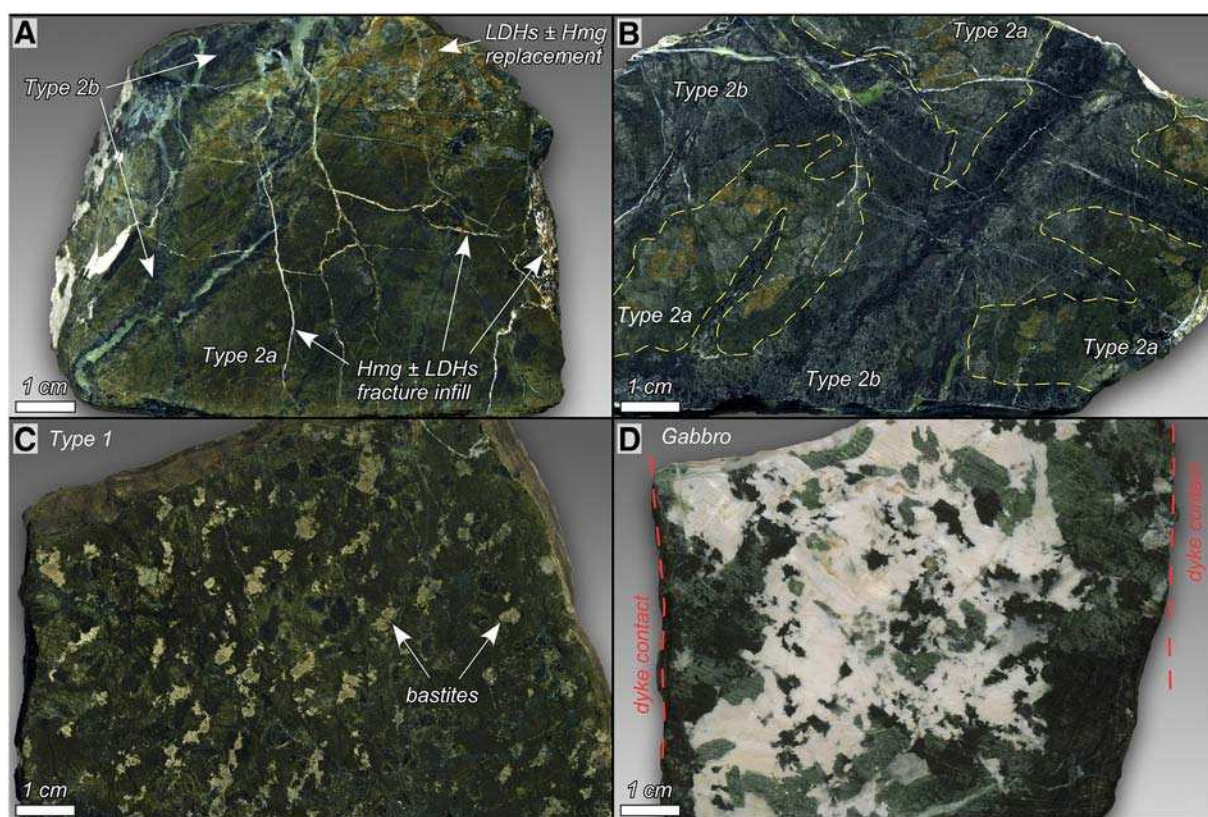


**Fig. 3.** Composite figure with representative polished slabs of the Montecastelli rock types. A) Type 2a serpentinized dunites; areas pervasively replaced by LDHs, orange-brown in colour; B) Relicts of Type 2a serpentinite embedded in a network of veins and replacement zones made of Srp, Mag and Fe-poor Brc (Type 2b serpentinized dunites); C) Example of pyroxene bearing serpentinized harzburgite (Type 1); D) A thin dyke of plagioclase-rich gabbro crosscutting serpentinized harzburgite. Abbreviations (here and in the next figures): Adr: andradite; Amk: amakinite; Bth: berthierine; Brc: brucite; Brg: brugnatellite; Chl: chlorite; Clg: Coalingite; Cdt: croenstedtite; Ftc: ferritchromite; Hmg: hydromagnesite; LDHs: Layered Double Hydroxides; Lsf: lansfordite; Mag: magnetite; Nsq: nesquehonite; Ol: olivine; Pyr: pyroaurite; Px: pyroxene; Pkv: pokrovskite; Pr-Hmg: proto-hydromagnesite; Srp: Serpentine; Spl: Mg-Al spinels; Tct: tochilinite. (For interpretation of the references to colour in this figure legend, the reader is referred to the web version of this article.)

2) a small mine dump located near the upper access of the Montecastelli mine.

### 3.1. The escarpment

The serpentinite outcrops are strongly fractured and several unstable escarpments with active rockfalls/landslides are widespread. The study area is characterized by a large and steep escarpment (slope area 30.000 m<sup>2</sup>; average height ~150 m), located on the western side of the Pavone River (Fig. 1). Here, the typical dark serpentinites are characterized by several spots of whitish carbonated zones (5–20 m<sup>2</sup>) cropping out at different elevations. The lowermost and easily accessible whitish outcrop was selected for this study. It is represented by a decametric hillock with persistent spring water issuing at its top (Fig. 4). The spring water partially percolates through the fractures of the underlying serpentinite body significantly wetting the rock and the newly formed carbonates, also during the dry seasons.

The carbonated hillock consists of highly fractured serpentinized dunites (Type 2), steeply embedded in serpentinized harzburgites (Type 1). External surfaces and fractures are coated and filled by variable amounts of whitish hydrous Mg-carbonates (mainly hydromagnesite with minor nesquehonite), orange-brown Fe-Mg Layered Double Hydroxides (LDHs; pyroaurite-coalingite) and aragonite (Figs. 4, 5 and S1). Precipitation of carbonates and LDHs is strongly variable, from very thin coatings to dense, massive and pervasive encrustations and fracture infillings. The most fractured rocks are affected by the thickest hydrous Mg-carbonate infill. Serpentinized harzburgites all around the carbonated hillock (Fig. 5D) show thin hydrous Mg-carbonates as external coatings,

together with the occurrence of large prismatic aragonite crystals, partially filling wide fractures. Aragonite is significantly less abundant compared to the Mg-rich carbonates.

Each year landslides remove several hundred m<sup>3</sup> of the escarpment, producing a progressive retreat of the slope surface. These landslides, together with the digging activity of mineral collectors, continuously expose dark and “fresh” surface of serpentinite. Periodic surveillance of the outcrops indicates that the newly exposed surface becomes coated by hydrous Mg-carbonate in only a few weeks to months.

For this study, representative samples of serpentinized dunites (Type 2) and harzburgites (Type 1), as well as of the three types of carbonate occurrences were collected. Water samples from the spring issuing at the top of the hillock and other serpentinite-hosted spring waters in the nearby areas were collected for chemical characterization, as reported in Boschi et al. (2013a).

### 3.2. The mine dump

The majority of the underground works of the Montecastelli mine were developed between 1842 and 1890, while during the 20th century exploration/exploitation activities were strongly reduced. The exploration of the Cu-Fe ore deposit during the 19th century was conducted by excavating crosscut drifts and level adits throughout large volumes of barren rocks and mineralized cataclastic rocks. In spite of the negligible ore production, a large amount of rock waste was produced and accumulated in mine dumps near the entrance of the main adits. Most of the mine dumps were formed ca. 150 years ago and, in many cases, were progressively covered by a





**Fig. 4.** Composite figure of the carbonated outcrops: A) Serpentinite-dominated escarpment showing at its top the carbonated hillock and the spring; B) Close-up view of the carbonated hillock; C) Example of the complex carbonate vein network and carbonate crusts characterizing the carbonated hillock; D) Distal part of the carbonated mining dump; E) Example of serpentinite clasts coated by hydrous Mg carbonates in the mining dump.

thin layer of soil and locally colonized by vegetation (oak trees). The small dump at the entrance of the uppermost crosscut adit (Santori adit; 245 m a.s.l.) has been recently flooded and eroded by a creek that exposed a vertical section where the complete stratigraphy, down to the substratum, is recorded. The dump is about 100 m<sup>2</sup> wide and up to 6 m thick (Fig. 2). It can be schematically divided into three layers:

- (i) The bottom layer, 1 to 4 m thick, is made up of large clasts of serpentinized harzburgites (Type 1; up to 60 cm in diameter) with large voids between clasts. This layer probably resulted from the excavation of the barren host rocks at the footwall of the orebody;

- (ii) The intermediate layer, ranging from 10 cm to 1 m in thickness, that consists of clasts of the barren serpentinite host (dunites and minor harzburgites; Type 2 and 1), the cataclastic zone and Cu–Fe sulphide ore set in a very fine- to fine-grained matrix of similar composition (Fig. 4E);
- (iii) The uppermost layer, 15–40 cm thick, is made up of poorly developed soil, alternating with minor quantities of serpentinized harzburgite clasts (Type 1) and tree roots.

On the distal part of the mine dump the bottom layer disappears and the intermediate layer contains less large clasts that become more fine-grained, while the upper layer has been largely removed by erosion (Fig. 4D).



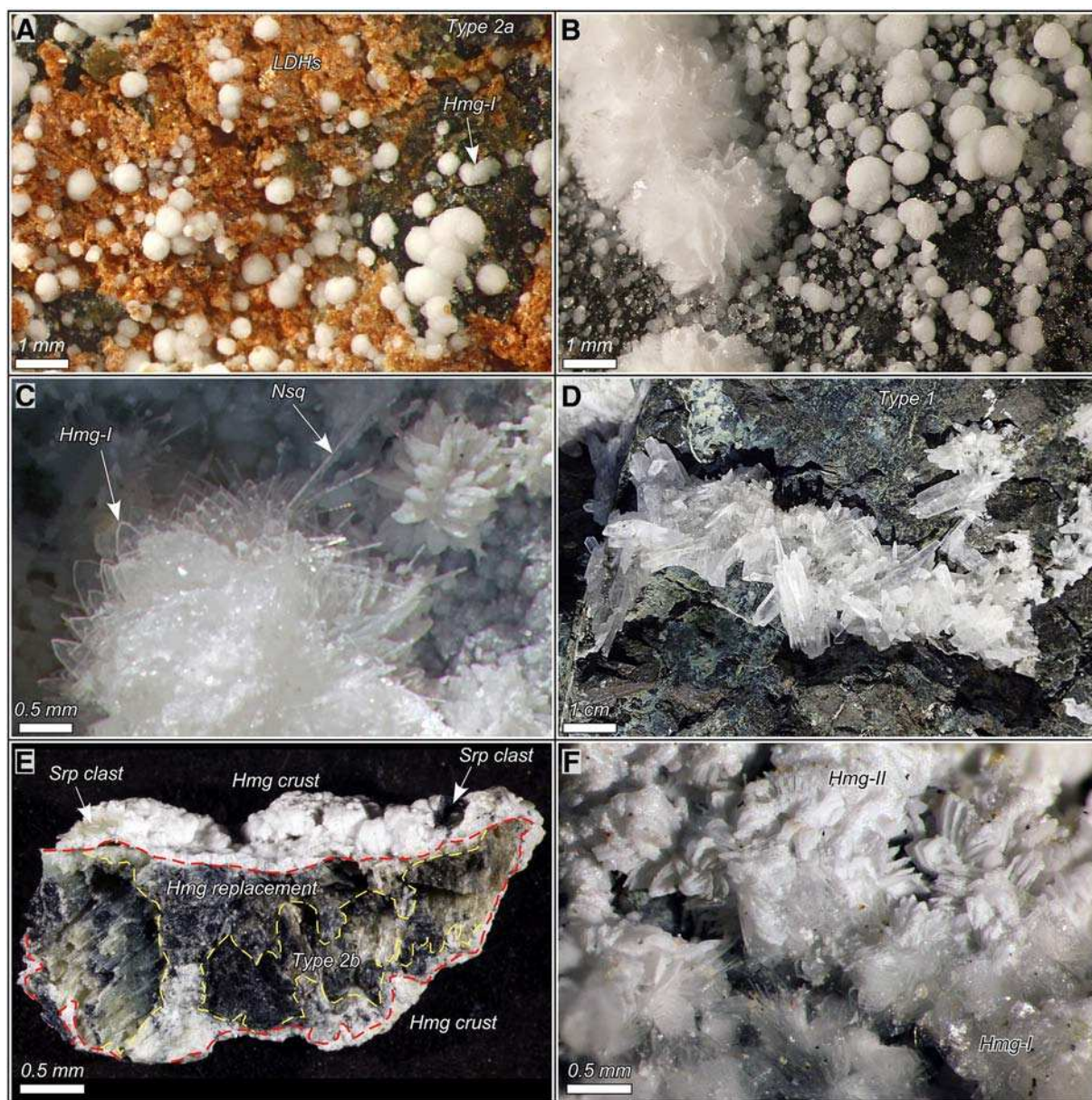


**Fig. 5.** Macroscopic images of idiomorphic crystals/aggregates of carbonates from Montecastelli. A) Close-packed rosettes of early hydromagnesite growing on LDHs and serpentinite host; fracture from Type 2a serpentinitized dunite; B) Different aggregates of early hydromagnesite: larger loosely-packed rosettes of lenticular crystals on top of smaller close-packed rosettes; fracture from Type 2b serpentinitized dunite; C) Tiny needles of nesquehonite implanted on a rosette made of sharp hydromagnesite blades; fracture from Type 2b serpentinitized dunite; D) Prismatic crystals of aragonite from a large fracture in serpentinitized harzburgite (Type 1); E) Serpentinitized dunite clast (Type 2b) partially altered to hydromagnesite. On the surface, a mm rosette-shaped hydromagnesite crust is formed; F) Early precipitation of hydromagnesite (Hmg-I) overprinted by a late hydromagnesite coating (Hmg-II).

The whitish incoherent intermediate layer, as well as the distal part of the mine dump, are characterized by widespread friable aggregates of hydrous Mg-carbonates coating the surface of serpentinite clasts and forming the fine-grained matrix, that acts as a weak cement. Most of the serpentinitized dunite clasts (Type 2) show tiny fractures filled by LDHs and hydrous Mg-carbonates. Clasts derived from the mineralized cataclastic zone (gabbro, Cu-Fe sulphides, fault gouge) are less affected by the precipitation of hydrous Mg-carbonates. Sampling activity and erosion locally exposed dark and fresh surfaces from broken serpentinite clasts. The newly exposed surfaces, as observed for the escarpment area, become coated by hydrous Mg-carbonates in few weeks to months.

We selected representative samples of clasts and matrices from the intermediate layer for a detailed mineralogical, petrographic and geochemical study of the hydrous Mg-carbonate precipitates and of the different clast rock types.

#### 4. Petrography, mineral chemistry and geochemistry of host rocks

Here we present the petrographic and geochemical characteristics together with EPM analyses of pyroxene-bearing serpentinitized harzburgites, the Type 1 serpentinite, and of serpentinitized dunites, the Type 2 serpentinite (Figs. 2, 3 and 6). Analytical methods are reported in the Supplementary Material (SM).

##### 4.1. Type 1 – serpentinitized harzburgites

Serpentinitized harzburgites show a high degree of serpentinization (>95%); relicts of clinopyroxene and orthopyroxene, with clinopyroxene exsolution lamellae parallel to the (001) plane, and primary Mg–Al-spinels, variably replaced by chromian-magnetite are observed. The lack of pyroxene peaks in XRD spectra suggests that the occurrence of relicts is probably less than 5% by volume.



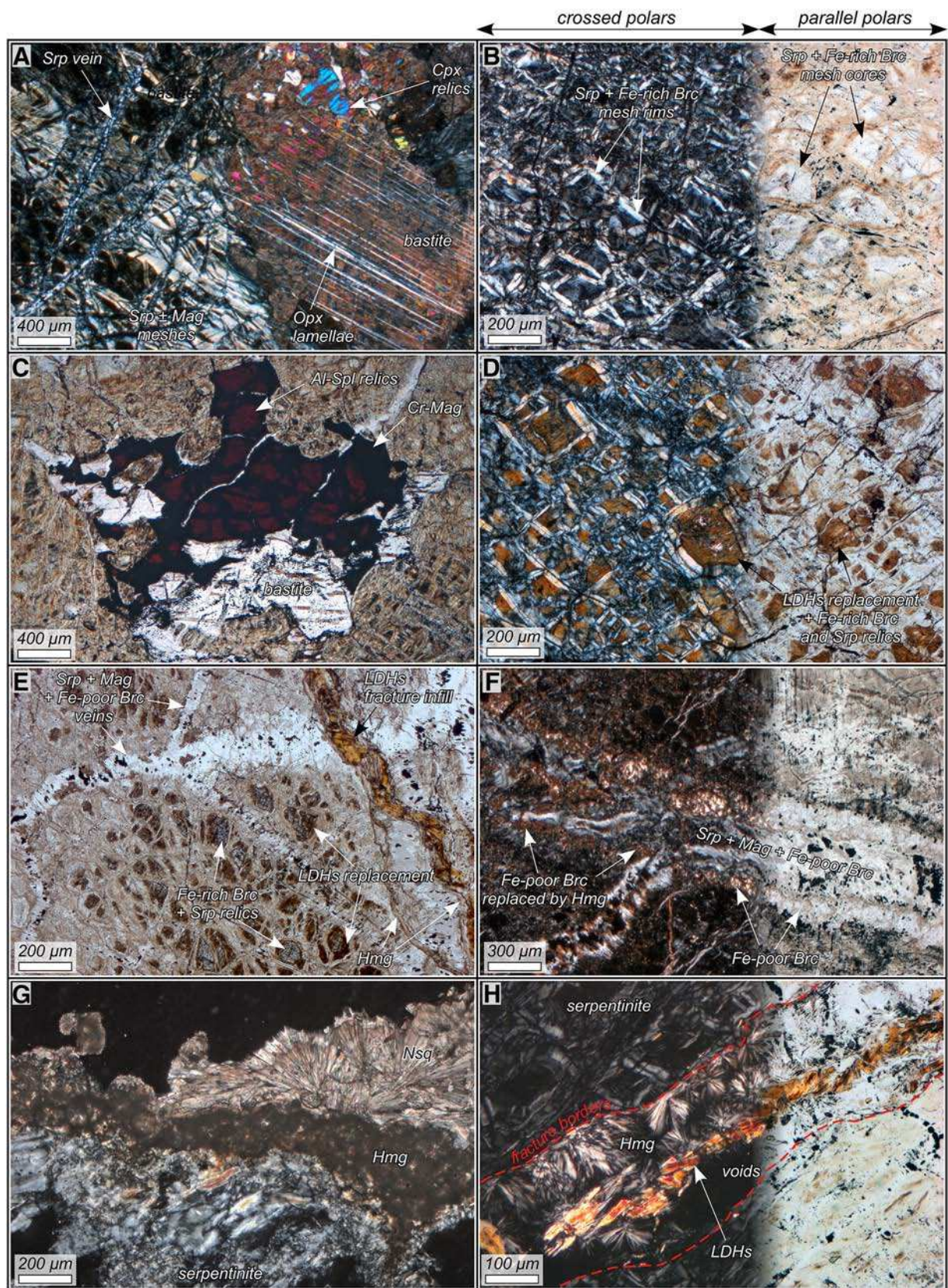


**Fig. 6.** Representative textural details of the main rock types (optical microscopy): A) Serpentinized harzburgite (Type 1) showing a bastite (with cpx and opx relicts) surrounded by mesh-textured serpentine matrix and cut by late serpentine veins, crossed polars; B) Mesh-textured serpentinitized dunite (Type 2a). Srp + Fe-rich Brc mesh cores are colourless in plain polarized light; C) A Mg–Al Spl – bastite cluster in mesh-textured Type 2a serpentinites: primary Spl is partially replaced by secondary Ftc, plain polarized light; D) Srp + Fe-rich Brc mesh cores/rims deeply replaced by orange-brown LDHs in Type 2a serpentinitized dunite; E) Textural relationships between Type 2a meshes, Type 2b Srp + Mag + Fe-poor Brc veins and recent fractures filled by LDHs and Hmg, plain polarized light; F) Large domains of Fe-poor Brc in a Type 2b veins; note Hmg selectively replacing Brc; G) Nsq rosettes growing on top of early Hmg comb crust, crossed polarized light; H) A typical fracture filled by LDHs + Hmg in Type 2a serpentinitized dunite. Abbreviations as in Fig. 3. (For interpretation of the references to colour in this figure legend, the reader is referred to the web version of this article.)



The secondary mineral assemblage is dominated by serpentine  $\pm$  magnetite. XRD, SEM-EDS, EPMA and micro-Raman investigations indicate that brucite is absent (both in veins and in serpentine mesh cores/rim). Magnetite occurs as grains in the mesh matrix as well as in late veins. Serpentine (from mesh cores, rims and veins) has a variable composition, comparable with serpentines from other Tuscan harzburgites but with lower iron content (Table S1, Fig. 7). Bastites display higher  $\text{Al}_2\text{O}_3/\text{SiO}_2$  and  $\text{FeO}/\text{MgO}$  ratios indicative of a significant berthierine component ( $\text{Fe}^{2+}, \text{Fe}^{3+}, \text{Al}$ ) $_3(\text{Si}, \text{Al})_2\text{O}_5(\text{OH})_4$ .

Brucite-free serpentinized harzburgites are geochemically distinct from serpentinized dunites, overlapping with the compositional field of harzburgitic–lherzolitic rocks (Table S2, Fig. 8) at distinctly higher  $\text{Al}_2\text{O}_3/\text{SiO}_2$  ( $>0.03$ ) and lower  $\text{MgO}/\text{SiO}_2$  ( $<1.05$ ) ratios.

The sampled rocks do not show evidence of Mg carbonation at a microscopic scale, as either replacement or fracture infill. Accordingly, geochemical analyses do not show any detectable carbon (Table S2, Fig. 9). Coatings and crusts of hydrous Mg carbonates have only been observed at the exposed surfaces of these rocks and around clasts in the mining dump.

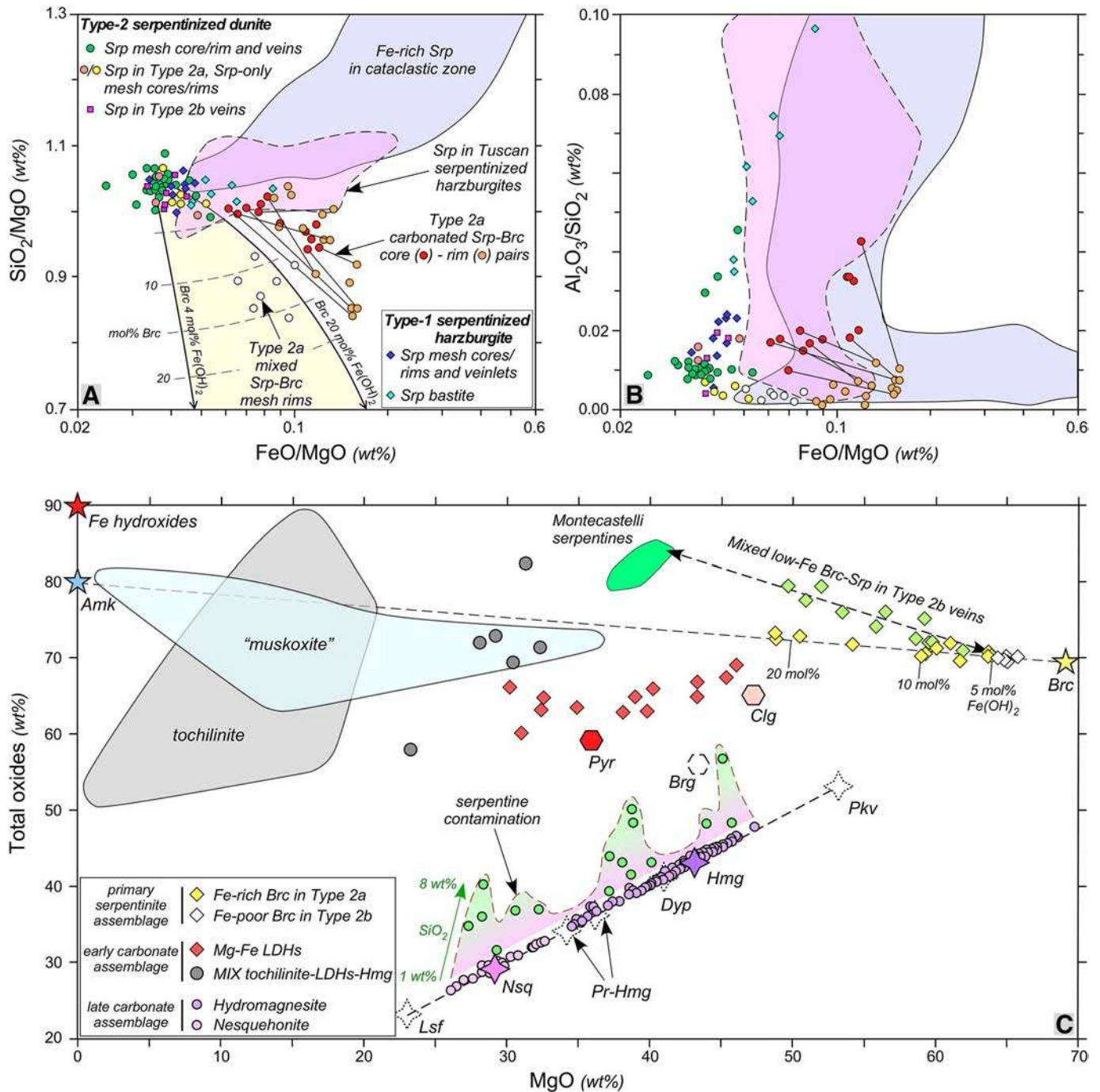


**Fig. 7.** Chemical variability of serpentine minerals (A and B), carbonates and brucites (C) from Montecastelli. Violet field range (7A and 7B) shows the different composition of the Al-Fe rich serpentines from the cataclastic rocks (data from Bedini, 2016). In Fig. 7A and B white circles report the mixed Srp–Brc analyses from Type 2a serpentinite mesh rims. Carbonated Srp–Brc rim mixed analyses (orange circles) plot higher  $\text{FeO}/\text{MgO}$  (wt%) and higher  $\text{SiO}_2/\text{MgO}$  (wt%) compared to the unaltered analyses (i.e. not-carbonated, white circles). This shift is due to a loss in Mg during brucite alteration to LDHs. See text and Tables 1, 2, S1 and S2 for more details; Abbreviations as in Fig. 3.



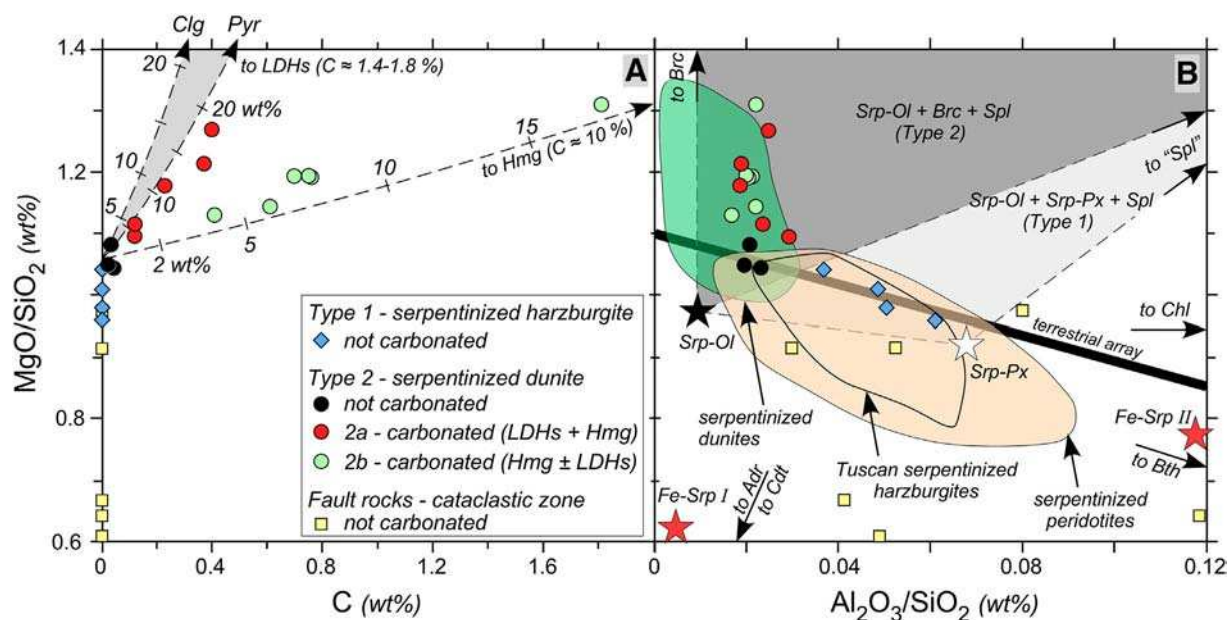















**Fig. 8.** Diagrams showing the chemical composition of whole rocks: A) Carbon content vs. MgO/SiO<sub>2</sub>. Note the distinct trends defined by Type 2a and Type 2b serpentinized dunites; B) MgO/SiO<sub>2</sub> vs Al<sub>2</sub>O<sub>3</sub>/SiO<sub>2</sub> diagram showing the different compositions of the Montecastelli samples together with other Tuscan serpentinites (from Boschi et al., 2009; Langone et al., 2013; Mellini et al., 2005;). It is worth noting that serpentinized dunite bodies have not yet been described from other outcrops in Tuscany. They probably represent a peculiar character of the Montecastelli outcrops (Anselmi et al., 2000; Boschi et al., 2009; Mellini et al., 2005; Rumori et al., 2004; Tribuzio et al., 2004). The terrestrial array line (Hart and Zindler, 1986; Jagoutz et al., 1979; Niu, 2004), is shown together with the variation field of serpentinized peridotites and dunites (Boschi et al., 2013b; Godard et al., 2008 and references therein). Black arrows represent mineralogical vectors pointing to the minerals that are relevant for the studied samples. Shades of grey highlight the distinct mineralogical assemblages for dunites and peridotites. Abbreviations as in Fig. 3.

#### 4.2. Type 2 – serpentinized dunites

In these samples serpentinization is pervasive (almost 100%) and only some Mg–Al-spinel relicts survived. This rock type is dominated by two main textural sub-types, both containing

large amounts of brucite (Figs. 3 and 6; following Wicks and Whittaker, 1977):

- Type 2a – characterized by pseudomorphic serpentine (after olivine) + Fe-rich brucite + magnetite associated with serpentine veins;

Rock type	Textural type	Replacement	Fracture infill	Coating
serpentinized dunite	Type 2a	 LDH  Hmg	 Tct  Nsq	
	Type 2b	 	  	
serpentinized harzburgite	Type 1		 Arg	

LDH

Layered Double Hydroxides

Tct

Tochilinite:  $6\text{Fe}_{1-x}\text{S} \cdot 5[(\text{Mg}, \text{Fe}^{2+})(\text{OH})_2]$ ; monoclinic (P2)

Hmg

Hydromagnesite:  $\text{Mg}_5(\text{CO}_3)_4(\text{OH})_2 \cdot 4\text{H}_2\text{O}$ ; monoclinic ( $\text{P2}_1/\text{c}$ )

Nsq

Nesquehonite:  $\text{MgCO}_3 \cdot 3\text{H}_2\text{O}$ ; monoclinic ( $\text{P2}_1/\text{m}$ )

Arg

Aragonite:  $\text{CaCO}_3$ ; orthorhombic (Pmcn)

$\left\{ \begin{array}{l} \text{Pyroaurite: } \text{Mg}_6\text{Fe}^{3+}_2(\text{OH})_{16}[\text{CO}_3] \cdot 4\text{H}_2\text{O}; \text{ rhombohedral (3R1)} \\ \text{Coalingite: } \text{Mg}_{10}\text{Fe}^{3+}_2(\text{OH})_{24}[\text{CO}_3] \cdot 2\text{H}_2\text{O}; \text{ rhombohedral (R32m)} \end{array} \right.$

**Fig. 9.** Mineral composition of the hydrous Mg carbonates and the layered double hydroxides (LDHs) observed at Montecastelli. The sketch shows the sequence of precipitation and the minerals abundance in the three different modes of occurrence (replacement, fracture infill and coating), and in the three lithologies.



- Type 2b – characterized by non pseudomorphic serpentine + Fe-poor brucite + magnetite associated with serpentine-brucite-magnetite veins.

The Type 2a dunite shows a serpentine + brucite mesh-textured matrix that ranges in colour from colourless to greenish-brownish to orange-brown (Fig. 6 B, D and E). Brucite is found in both mesh cores and rims, although rarely visible under the microscope (Fe-rich brucite is colourless in transmitted light, Fig. 6B). Its presence, as intimate sub-microscopic mixture in serpentine rims/cores and as discrete grains in cores, was ascertained by XRD, microRaman and EPM analyses (Figs. S2, S3 and S4; Tables 1 and S3). Serpentine + brucite occur in mesh cores as irregular aggregates, while in the mesh rims they show an apparently fibrous pattern at high angle to the original fracture. Magnetite occurs as disseminated small grains, in cores, in the external part of the rims and in small late serpentine veins. Sometimes, meshes formed only by serpentine have been observed.

In contrast to the serpentinized harzburgite, Type 2a shows clear evidences of diffusive carbonation, macroscopically marked by a change in colour from dark-green/black to brownish (Fig. 3A and B). At a microscopic scale, Fe-rich brucite is extensively replaced by Mg-Fe LDHs in mesh cores and rims (orange-brown in thin sections, Fig. 6D and E). In transmitted light Mg-Fe LDHs display a strong pleochroism (colourless to orange-brown; Fig. 6D, E, H) and a medium-high birefringence. They can be easily distinguished from brucite that, also at the highest Fe-rich composition (20 mol.% Fe(OH)<sub>2</sub>), is colourless, not pleochroic and very low in birefringence (Fig. 6B, D, F). In addition, small fractures (aperture up to ca. 1 mm) are filled by orange-brown Mg-Fe LDHs and minor amount of white hydrous Mg carbonates (Figs. 5A and 6E).

The Type 2b dunite appears as an overprinting texture of the Type 2a dunite. It shows a network of serpentine-Fe-poor brucite-magnetite veins (up to a few mm thick) surrounded by two symmetric reaction bands that pervasively recrystallize the Type 2a pseudomorphic texture (Figs. 3B and 6 E-F). Relicts of Type 2a serpentinite usually exist between the reaction bands, but locally the replacement process goes to completion. Magnetite is abundant, as very tiny grains (few  $\mu\text{m}$ ) in the veins and in the first portion of the reaction bands. In the inner part of the replacement domains, magnetite occurs as a few (1 to 3) large grains (up to 5 mm). Bands with large disseminated magnetite are almost black, while the intervening domains with a few large magnetite grains are pale green to yellow, approaching the translucent character of the so-called “noble serpentine”. Fe-poor brucite (either

finely disseminated or as patches) is intergrown with serpentine and magnetite both in veins and in replacement domains (Figs. 6F).

Here, the extensive carbonation could be noted as a whitening of the original blackish magnetite-rich rock (Figs. 3B and 6E). In fact, in this rock-type, Fe-poor brucite is pervasively altered to hydrous Mg carbonates (LDHs are scarce; Fig. 6E and F).

Serpentine from both rock types shows an overall Fe-poor composition (FeO<sub>tot</sub> < 2.2 wt.%; Fig. 7, Table S1), high Mg# (97 in average) and variable analytical totals (between 81 and 85 wt.%). The latter feature is well known in the literature, although not emphasized (e.g., Frost et al., 2013; Klein et al., 2009; 2014; Möll et al., 2007). This can be attributed either to a higher water content in the serpentine structure (up to 20 wt.% instead of the theoretical 13 wt.%; Table S1; see D’Antonio and Kristensen, 2004) or to a micro-porous texture with nanometric voids (possibly due to brucite dissolution; Jöns et al., 2017).

Type 2a brucite (in mesh-cores and veinlets) shows a high FeO content (Fe-rich brucite; 5 < Fe(OH)<sub>2</sub> < 22 mol.%). Type 2b brucite is Fe-poor, with Fe(OH)<sub>2</sub> < 5 mol.% (Fig. 7C, Tables 1 and S3). The sub-microscopic Fe-rich brucite-serpentine mixtures in the mesh rims (Type 2a dunite) are confirmed by EPM analyses that plot at intermediate compositions (white circles in Fig. 7A). At the same time, a number of analyses plot between the Fe-brucite and LDHs endmembers (not shown in Fig. 7C; see Table S3), indicating a partial brucite replacement by LDHs. The difficulty of interpreting and processing the EMP analyses is well shown by Fe-rich carbonated serpentine-brucite mixture analyses, plotted as an example in Fig. 7A. Similar occurrences of brucite, variably enriched in iron, have been documented in oceanic (Bach et al., 2006; Klein et al., 2009; 2014), forearc (D’Antonio and Kristensen, 2004) and ophiolitic serpentinites (Baronnet and Boudier, 2001; Frost et al., 2013; Langone et al., 2013; Mumpton and Thompson, 1966). Bulk rock analyses of Type 2 serpentinites show high MgO/SiO<sub>2</sub> (>1) coupled to low Al<sub>2</sub>O<sub>3</sub>/SiO<sub>2</sub> (<0.03) ratios, confirming a dunitic nature of the protolith (Fig. 8, Table S2). They fall mostly into the dunite field range, at the intersection with the harzburgite-lherzolite field.

Analyses of carbon content (after careful removal of any carbonate crust and filled fractures) indicate that most of the samples (excluding three samples; i.e. black circles in Fig. 8A) have an elevated and variable carbon content (TIC ranging between 0.1 and 1.8 wt.%; Table S2 and Fig. 8A). In more detail, the Type 2a and the Type 2b dunites display two distinct positive correlations between C and MgO/SiO<sub>2</sub> ratios. Type 2a (LDHs-rich) samples show a steeper correlation against MgO/SiO<sub>2</sub> ratio, with a limited increase of carbon content. Type 2b samples

**Table 1**  
Representative EPM analyses of brucite from Montecastelli.

Mineral	Brucite														
Rock type	Serpentinized dunites														
Location	Escarpment								Dump						
Sample	TP01	TP01	TP01	TP101	TP101	TP101	TP103	TP103	TP109	TP109	TP109	TP109	TP120	TP120	TP120
(wt.%)															
SiO <sub>2</sub>	0.08	0.28	1.04	0.60	1.18	0.42	0.12	0.04	1.22	0.59	1.08	0.79	0.34	0.50	0.19
TiO <sub>2</sub>	<d.l.	<d.l.	<d.l.	<d.l.	<d.l.	<d.l.	<d.l.	<d.l.	0.09	<d.l.	<d.l.	0.12	0.08	0.06	<d.l.
Al <sub>2</sub> O <sub>3</sub>	<d.l.	<d.l.	<d.l.	0.06	0.11	<d.l.	0.07	<d.l.	0.09	0.86	<d.l.	0.15	0.12	0.15	0.18
Cr <sub>2</sub> O <sub>3</sub>	<d.l.	0.08	<d.l.	<d.l.	<d.l.	<d.l.	<d.l.	<d.l.	<d.l.	<d.l.	<d.l.	<d.l.	0.07	<d.l.	<d.l.
FeO	3.85	4.53	4.56	9.04	8.48	5.72	4.84	4.11	5.53	9.13	14.69	8.85	21.68	19.94	21.45
MnO	0.36	0.38	0.32	0.51	0.54	0.53	0.30	0.45	0.28	0.38	0.65	0.30	0.68	0.70	0.90
MgO	65.05	63.73	63.91	61.05	58.99	63.71	64.90	64.82	61.69	60.08	54.21	59.31	48.78	50.50	48.84
NiO	0.14	0.72	0.52	0.22	0.09	0.04	<d.l.	0.13	0.08	0.06	0.52	0.08	0.35	0.34	0.38
CaO	<d.l.	<d.l.	<d.l.	<d.l.	0.04	<d.l.	0.03	<d.l.	<d.l.	0.04	0.48	0.04	0.39	0.27	0.41
Na <sub>2</sub> O	<d.l.	<d.l.	<d.l.	<d.l.	<d.l.	<d.l.	<d.l.	<d.l.	<d.l.	<d.l.	<d.l.	<d.l.	<d.l.	<d.l.	<d.l.
K <sub>2</sub> O	<d.l.	0.36	<d.l.	0.25	0.04	0.32	<d.l.	0.15	<d.l.	<d.l.	<d.l.	0.33	0.82	0.20	<d.l.
SO <sub>3</sub>	<d.l.	<d.l.	<d.l.	0.09	0.06	<d.l.	<d.l.	<d.l.	<d.l.	0.07	<d.l.	0.06	<d.l.	0.12	0.09
Cl	<d.l.	<d.l.	<d.l.	<d.l.	<d.l.	<d.l.	<d.l.	<d.l.	<d.l.	<d.l.	<d.l.	<d.l.	<d.l.	<d.l.	<d.l.
Total	69.48	70.08	70.35	71.82	69.53	70.74	70.26	69.70	68.98	71.21	71.63	70.03	73.31	72.78	72.44
mol.% Fe(OH) <sub>2</sub>	3.2	3.8	3.8	7.7	7.5	4.8	4.0	3.4	4.8	7.9	13.0	7.7	20.0	18.1	19.8
mol.% Mg(OH) <sub>2</sub>	96.8	96.2	96.2	92.3	92.5	95.2	96.0	96.6	95.2	92.1	87.0	92.3	80.0	81.9	80.2

<d.l. = < detection limit.



**Table 2**

Representative EPM analyses of Mg–Fe layered double hydroxides (pyroaurite–coalingite) from Montecastelli.

Mineral	Pyroaurite ←	Pure LDH					→ Coalingite
Rock type	Serpentinized dunites						
location	Escarpment	Dump	Dump	Dump	Dump	Dump	
Sample	TP02b	TP101	TP120	TP109	TP120	TP109	
Analytical point	1	3	11	8	10	9	
(wt.%)							
SiO <sub>2</sub>	0.32	<d.l.	0.78	0.23	0.18	0.77	
TiO <sub>2</sub>	<d.l.	<d.l.	<d.l.	0.07	<d.l.	<d.l.	
Al <sub>2</sub> O <sub>3</sub>	0.16	0.05	0.17	0.17	0.23	0.43	
Cr <sub>2</sub> O <sub>3</sub>	<d.l.	0.07	<d.l.	<d.l.	<d.l.	<d.l.	
FeO	24.64	23.35	21.34	19.29	19.67	15.84	
MnO	0.09	1.82	2.24	2.66	0.64	0.62	
MgO	38.98	40.25	38.14	39.79	43.31	46.53	
NiO	0.16	0.05	<d.l.	<d.l.	0.16	<d.l.	
CaO	<d.l.	0.04	<d.l.	<d.l.	0.07	<d.l.	
Na <sub>2</sub> O	<d.l.	<d.l.	<d.l.	<d.l.	<d.l.	<d.l.	
K <sub>2</sub> O	<d.l.	0.34	<d.l.	0.71	0.59	<d.l.	
SO <sub>3</sub>	0.52	<d.l.	0.12	<d.l.	<d.l.	0.09	
Cl	<d.l.	<d.l.	0.04	0.05	0.07	0.04	
Total	64.87	65.97	62.83	62.97	64.92	64.32	
mol.% coalingite	≈ 0	6	14	45	59	≈ 100	
mol.% pyroaurite	≈ 100	95	86	55	41	≈ 0	
Notes	Slight Fe excess Fe hydroxides?	Slight Fe excess Fe hydroxides?				Slight Mg excess	
Mineral	Mixed LDH-Fe hydroxides						
Rock type	Serpentinized dunites						
Location	Dump	Dump	Dump	Dump	Dump	Dump	
Sample	TP101	TP101	TP101	TP101	TP101	TP101	
Analytical point	2	6	7	5	4		
(wt.%)							
SiO <sub>2</sub>	0.07	0.10	0.12	0.11	0.13		
TiO <sub>2</sub>	<d.l.	<d.l.	<d.l.	<d.l.	<d.l.		
Al <sub>2</sub> O <sub>3</sub>	0.04	0.22	0.22	0.11	0.06		
Cr <sub>2</sub> O <sub>3</sub>	<d.l.	<d.l.	<d.l.	<d.l.	<d.l.		
FeO	25.65	27.91	27.06	30.37	32.15		
MnO	2.12	1.71	0.90	0.61	2.40		
MgO	34.91	32.42	31.05	32.58	30.23		
NiO	<d.l.	0.06	0.07	0.53	<d.l.		
CaO	0.12	0.24	0.16	0.22	0.27		
Na <sub>2</sub> O	0.07	0.11	0.05	0.11	0.1		
K <sub>2</sub> O	0.35	0.2	0.28	<d.l.	0.64		
SO <sub>3</sub>	0.18	0.19	0.22	0.13	0.16		
Cl	<d.l.	<d.l.	<d.l.	<d.l.	<d.l.		
Total	63.51	63.16	60.13	64.77	66.14		
mol.% coalingite	–	–	–	–	–		
mol.% pyroaurite	–	–	–	–	–		
Notes	Strong Fe excess – mixture of LDH with Fe hydroxides (?)						

&lt;d.l. = &lt; detection limit. wt.% = weight percent.

(rich in hydrous Mg carbonates) plot along a shallower trend with larger C increments. Accordingly, hydrous Mg carbonates contain similar amount of MgO, but have an order of magnitude higher C contents (ca. 10 wt.%) with respect to LDHs (1.4–1.8 wt.%).

Overall, petrographic and geochemical analyses point to a pervasive carbonation of the brucite-rich serpentinized dunites, affecting and partially replacing the inner portion of the rocks (Figs. 3A, B and 5). Nonetheless, the most spectacular carbonation effect is documented by the abundant precipitation of white, hydrous Mg carbonates ± Mg–Fe LDH (± very rare aragonite) as fracture infill and surface coatings/crusts (at outcrop free surfaces and around clasts in the mine dump). In the first case, hydrous Mg carbonates can produce thick crusts (up to 1 cm) made of fibrous-radiating spherules and/or comb aggregates of crystals. Textures and mineral chemistry of carbonate parageneses are described in detail in the next chapters.

## 5. Petrography and mineral chemistry of carbonate assemblages

### 5.1. Mg–Fe LDHs: replacement and fracture infill

The layered double hydroxides (LDHs) are characterized by structures in which brucite-like layers carry a net positive charge, due to the partial substitution of trivalent octahedrally coordinated cations (e.g. Fe<sup>3+</sup>, Al<sup>3+</sup>, Cr<sup>3+</sup>) for divalent cations (e.g. Mg<sup>2+</sup>), giving a general layer formula of [(M<sup>2+</sup><sub>1-x</sub>M<sup>3+</sup><sub>x</sub>)(OH)<sub>2</sub>]<sup>x+</sup> (Mills et al., 2012). The positive charge is balanced by a variety of anions (e.g. CO<sub>3</sub><sup>2-</sup>, SO<sub>4</sub><sup>2-</sup>), which are intercalated between the layers. LDHs show a wide range of polytypism–polysomatism (also at the scale of a single crystal) that, at a first instance, arises from the different ways the brucite-like layers can stack. For these reasons, LDHs characterization needs multiple methods involving XRD, TEM, mineral chemistry, Raman/IR spectroscopy, Mössbauer spectroscopy



and other techniques. In this contribution, LDHs were mainly characterized by optical microscopy, EPMA and micro-Raman (Figs. S3 and S4) but some grains were also separated for XRD characterization (X-ray diffraction patterns; see Analytical Methods in the Supplementary Material for details).

As mentioned previously, LDHs occur mainly in Type 2a serpentinized dunites and are less abundant in Type 2b (Figs. 5, 6 and 9). They are documented by  $\text{Mg}^{2+}$ – $\text{Fe}^{3+}$  carbonates showing chemical, spectroscopic and XRD characteristics ranging from pyroaurite to coalingite (Table 2, Figs. 7C, 9, S3 and S4). Both these minerals share similar rhombohedral symmetry, although the space groups are different (coalingite is R32m; pyroaurite has two polytypes 3R1 and 2H1). Coalingite ( $\text{Mg}_{10}\text{Fe}^{3+}_2(\text{OH})_{24}[\text{CO}_3] \cdot 2\text{H}_2\text{O}$ ) has 1/6 of the cations trivalent rather than 1/4 as in pyroaurite ( $\text{Mg}_6\text{Fe}^{3+}_2(\text{OH})_{16}[\text{CO}_3] \cdot 4\text{H}_2\text{O}$ ). Coalingite can also be described as a 1:1 interstratification of pyroaurite and brucite layers, giving alternating spacing between (Mg/Fe) planes along the *c* axis. Most of the Montecastelli XRD patterns are consistent with pyroaurite although their chemical composition (i.e. their MgO/MgO + FeO ratio; Table 2; Figs. S3 and 7C) ranges from coalingite to pyroaurite. In some samples, it spreads towards higher Fe-rich composition, similar to the questionable species “muskoxite” (see Mills et al., 2012). Under the laser beam, the Montecastelli Mg–Fe LDHs are rapidly deteriorated but produce Raman spectra that are easily distinguishable from those of brucite, serpentine and other potential LDHs such as hydrotalcite (Fig. S4).

Disseminated Mg–Fe LDHs (10–100  $\mu\text{m}$ ) in mesh cores (from Type 2a serpentinized dunites) preferentially replace Fe-rich brucite. Large relicts of brucite can be recognized in transmitted light, and tiny relicts of this mineral often survive also inside the LDH grains, as indicated by the occasional collection of mixed Raman spectra. LDHs also replace serpentine–brucite intergrowths in mesh rims. This process is not detectable in transmitted light, but is indicated by mixed serpentine–LDH–brucite Raman spectra and by the deviation of EPM analyses from the serpentine–brucite field towards the average composition of LDHs (Fig. 7A).

LDHs are also observed as infilling of tiny fractures in the rocks (Fig. 6E, H). Completely filled veins show a packed aggregate of subhedral

tabular prismatic crystals (100–500  $\mu\text{m}$ ) with typically strong pleochroism and cleavage cracks on (001). Sometimes the fractures were only partially filled and LDHs grew in open spaces as platelets with perfect euhedral morphology. Partially filled fractures and re-opened veins frequently record a later crystallization of hydromagnesite, as both delicate fibrous-radiating spray-like aggregates and fibrous aggregates oriented parallel to the vein boundaries (Figs. 5A and 6H). LDH crystals overgrown by hydromagnesite did not record any detectable alteration.

There is no systematic chemical variation between LDHs from dissemination and fracture infill, while LDH analyses with Fe excess have been measured in crystals from a re-opened vein showing late oxidation effects (Fig. 7C). Most of the LDH crystals from the latter vein are darker than usual. They show anomalous Raman spectra where the diagnostic coalingite–pyroaurite peak ( $526\text{ cm}^{-1}$ ) shows an irregular and flat shape, and in some cases no peaks at all.

Some LDH-hydromagnesite veins contain rosettes and fan-shaped aggregates of acicular crystals of an Fe–Mg mineral with a high sulphur and aluminium content (respectively  $\text{SO}_3 = 2.5$  to 15 wt.% and  $\text{Al}_2\text{O}_3$  0.3 to 2.59 wt.%; Fig. 10). The acicular, flattened crystals are tiny, usually less than 100  $\mu\text{m}$  in length, 1  $\mu\text{m}$  thick, and are black to dark-brown in colour, except those from oxidized veins that are orange-brown. Near the tips, they are frequently split and curved producing hooks and cylindrical geometries (Fig. 10B and D). These acicular aggregates nucleated on serpentine walls and on top of LDHs, and then they were eventually embedded at the core of later hydromagnesite rosettes (Fig. 10A). In reflected light, they show a distinct higher reflectance with respect to LDHs and hydromagnesite, in which they are hosted. Accurate chemical analyses were hampered by the thickness of the crystals, the intimate intergrowth with carbonates and by the variable oxidation to Fe-hydroxides. Micro-Raman provided in all cases mixed spectra showing the diagnostic peaks of LDHs ( $526\text{ cm}^{-1}$ ) and hydromagnesite ( $1100\text{ cm}^{-1}$ ) as well as some peaks around  $240\text{ cm}^{-1}$ ,  $300\text{ cm}^{-1}$  and  $360\text{ cm}^{-1}$ . The entire dataset is coherent with the poorly characterized mineral tochilinite, a hybrid, layered hydroxide–sulphide with the ideal formula  $6\text{Fe}_{1-x}\text{S} \cdot 5[(\text{Mg}, \text{Fe}^{2+})(\text{OH})_2]$  (Fig. 9). Its composition was established to be widely variable, primarily in cations from the hydroxide block, where a substantial admixture of Al was found in some

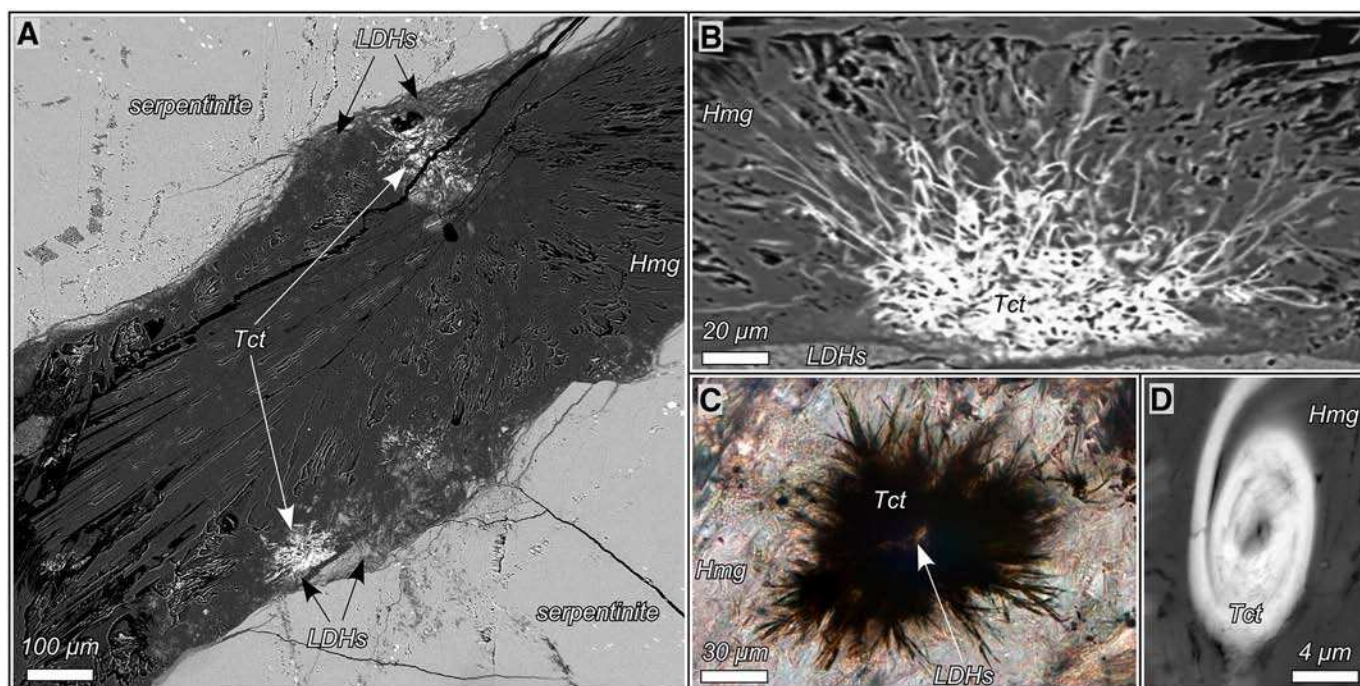


**Fig. 10.** SEM-BSE photos (A, B and D) and microscope photo (C) of probable tochilinite embedded in LDHs + Hmg. Note the textural position between early LDHs and later Hmg infill (a) and the typical curved cylindrical tips (d). Abbreviations as in Fig. 3.

samples (with generally predominant Mg) and Fe in samples that reach the composition of ferrotrochilinite (Aleksandrov and Senin, 2005; Jambor, 1976; Organova et al., 1988). In general, trochilinite is found in low temperature assemblages related to ultramafic rocks (Beard, 2000).

### 5.2. Hydrous Mg carbonates: replacement, fracture infill and free-surface coating

Hydrous magnesium carbonates are represented by hydromagnesite and nesquehonite. XRD, microRaman and EPMA data indicate that hydromagnesite is the most common phase at the escarpment and mine dump, while nesquehonite was identified in a few samples from the escarpment outcrop, typically associated with hydromagnesite (Figs. 9, S3 and S4). In nature, hydromagnesite is by far the most common (and the most stable under atmospheric conditions) mineral among the magnesium-hydrous carbonates, followed by the metastable nesquehonite (Akao et al., 1974). Both minerals form at ambient temperature ( $T > 15^\circ\text{C}$ ), although it is generally reported that nesquehonite is more readily formed at  $25^\circ\text{C}$ , particularly under relatively high  $\text{CO}_2$  pressures, while hydromagnesite occurs at comparatively higher temperatures (Gautier et al., 2014; Hanchen et al., 2008; Hopkinson et al., 2012). Hydromagnesite shows three different modes of occurrence both in the escarpment and the mine dump (Fig. 9):

- 1) Replacement of rock mass;
- 2) Infill in rock fractures;
- 3) Coating and encrustation at exposed surfaces.

- (1) The first carbonation occurrence mainly affects Type 2b serpentinized dunites (rich in Fe-poor brucite; Fig. 9). Replacement of brucite by hydromagnesite is macroscopically detectable on freshly broken, dry surfaces due to the whitening effect. Fine-grained, interpenetrating aggregates of hydromagnesite platelets (tens of  $\mu\text{m}$ ; low to medium birefringence) variably replace the brucite grains intergrown with serpentine and magnetite both in veins and in non-pseudomorphic aggregates (Fig. 6F). Rarely, fibrous-radiating aggregates of hydromagnesite were observed, which were identified using MicroRaman spectroscopy. When the crystal-size of hydromagnesite is extremely fine (less than a few  $\mu\text{m}$ ), light absorption is strong and carbonated domains have in plain polarized light a distinctive pale-brown colour. Locally, hydromagnesite replaces Fe-rich brucite in mesh cores in Type 2a relicts at the direct contact with the Type 2b veins. In this case, hydromagnesite is associated with abundant LDH grains.
- (2) Fractures of variable width (from hundred  $\mu\text{m}$  up to 1 cm) in both Type 2a and Type 2b serpentinized dunites host the second type of hydromagnesite (Fig. 9). In this case, hydromagnesite fills the fractures or occurs along fracture walls as continuous crust or isolated aggregates, leaving an open space in the axial zone (Figs. 5B and 6H). These crystals show variable size (from a few tens of  $\mu\text{m}$  to ca. 1 cm) and habits (flat needles, blades, platy/lenticular). They form a large variety of aggregates depending on nucleation substrate (fracture walls, previously formed hydromagnesite aggregates, tiny clasts of serpentinites filling the fissures), nucleation site density, and crystal packing.

In several samples, a recurrent textural evolution has been observed. An early precipitation of hydromagnesite (Hmg-I) starts with close-packed aggregates of flat needles, growing perpendicular to the fracture walls. They form continuous comb crusts (less than 1 mm in thickness) or isolated globules and/or botryoidal aggregates on the vein walls (Figs. 5A, B, E and 11A). Locally, the size of the crystals increases (up to 1 cm in length), and the aggregates become more loosely packed, producing different types of rosettes and 3D sprays made of either sharp blades (Figs. 5C and 11B) or lenticular crystals (Figs. 5B and 11A).

In fractures of Type 2a serpentinites, hydromagnesite can be associated with LDHs (Fig. 6E, H) and rarely with trochilinite (Figs. 9 and 10). In these cases, LDH is the first precipitating phase, followed by trochilinite and then by hydromagnesite. In fractures of Type 2b serpentinites, hydromagnesite is the only detectable phase (Fig. 5B–C). Nesquehonite was rarely identified and occurs as scattered tiny prismatic crystals and loosely packed aggregates of relatively thick columnar crystals, growing on top of hydromagnesite aggregates (2D radiating, and 3D sprays; 10–20  $\mu\text{m}$  thick, 40–80  $\mu\text{m}$  long; Figs. 5C and 6G). The single magnesium-free mineral found in this occurrence is aragonite, whose 3D sprays of tiny needles have been very rarely observed as a pre-hydromagnesite precipitate.

- (3) Finally, the third occurrence takes place at exposed surfaces of outcrops (escarpment, Type 1 and 2 serpentinites; Fig. 9) and around clasts from the internal voids of the mine dump (both Type 1 and Type 2 serpentinites). The carbonate precipitation follows that same textural evolution as previously described for the occurrence 2. More or less continuous hydromagnesite crusts, with variable thickness and external surface morphology (from planar to botryoidal) could be associated with minor LDHs and rare nesquehonite (Figs. 5, 11 and S5).

Sometimes a late additional hydromagnesite precipitation (Hmg-II) produces fragile and earthy coatings (thickness up to few tens of  $\mu\text{m}$ ) that are easily pulverized between the fingers (Figs. 5F and 11D). The coating is made of irregular aggregates of tiny equant or slightly elongated hydromagnesite crystallites (50–800 nm), occasionally associated with serpentine fibres (0.5–4  $\mu\text{m}$ , Fig. 11E). Locally, some crystallites increase in size (up to few  $\mu\text{m}$ ) producing platy morphologies and merging into a continuous, apparently, smooth surface that mantle earlier hydromagnesite rosettes (Fig. 11F).

In the mine dump, voids between clasts are partially filled by a fine-grained serpentinite matrix that is usually cemented by hydromagnesite. The resulting microbreccia-like aggregate is made of a 3D aggregate (botryoidal) of tiny rosettes having numerous inclusions and small seed-like serpentinite clasts. All these aggregates are made of tiny lenticular/platy crystals (up to 10  $\mu\text{m}$  in size).

Chemical compositions of hydrous Mg carbonates (Fig. 7C) are consistent with those of hydromagnesite and nesquehonite, although some scattering suggests the presence of metastable phases (such as the so-called proto-hydromagnesite). Contamination by serpentine clasts/powder is indicated by some EPM analyses that deviate from the general trend (Table S4).

## 6. Discussion

The geochemical and mineralogical data presented here indicates that the present-day, selective carbonation at Montecastelli is controlled by the different mineralogical assemblage of the serpentinized mantle rocks. Here, we briefly discuss the origin of the distinct serpentinite mineral assemblages, highlighting the mechanism of Fe-rich and Fe-poor brucite formation. Based on our mineral data, we derive the main chemical reactions responsible for carbonation at Montecastelli, and link the brucite composition to the carbonation products and to the CCS efficiency.

### 6.1. The serpentinization process

The mineral assemblage of serpentinized dunites (Type 2) is dominated by Al-poor/Mg-rich serpentine and brucite, variably enriched in iron. Serpentinized harzburgites (Type 1) are brucite-free and contain both mesh-textured serpentine and bastite (more aluminous and relatively Fe-rich; Fig. 7A and B). The different mineralogical parageneses and variations in mineral chemistry are roughly correlated to the bulk composition of the serpentinite types (Fig. 8B).



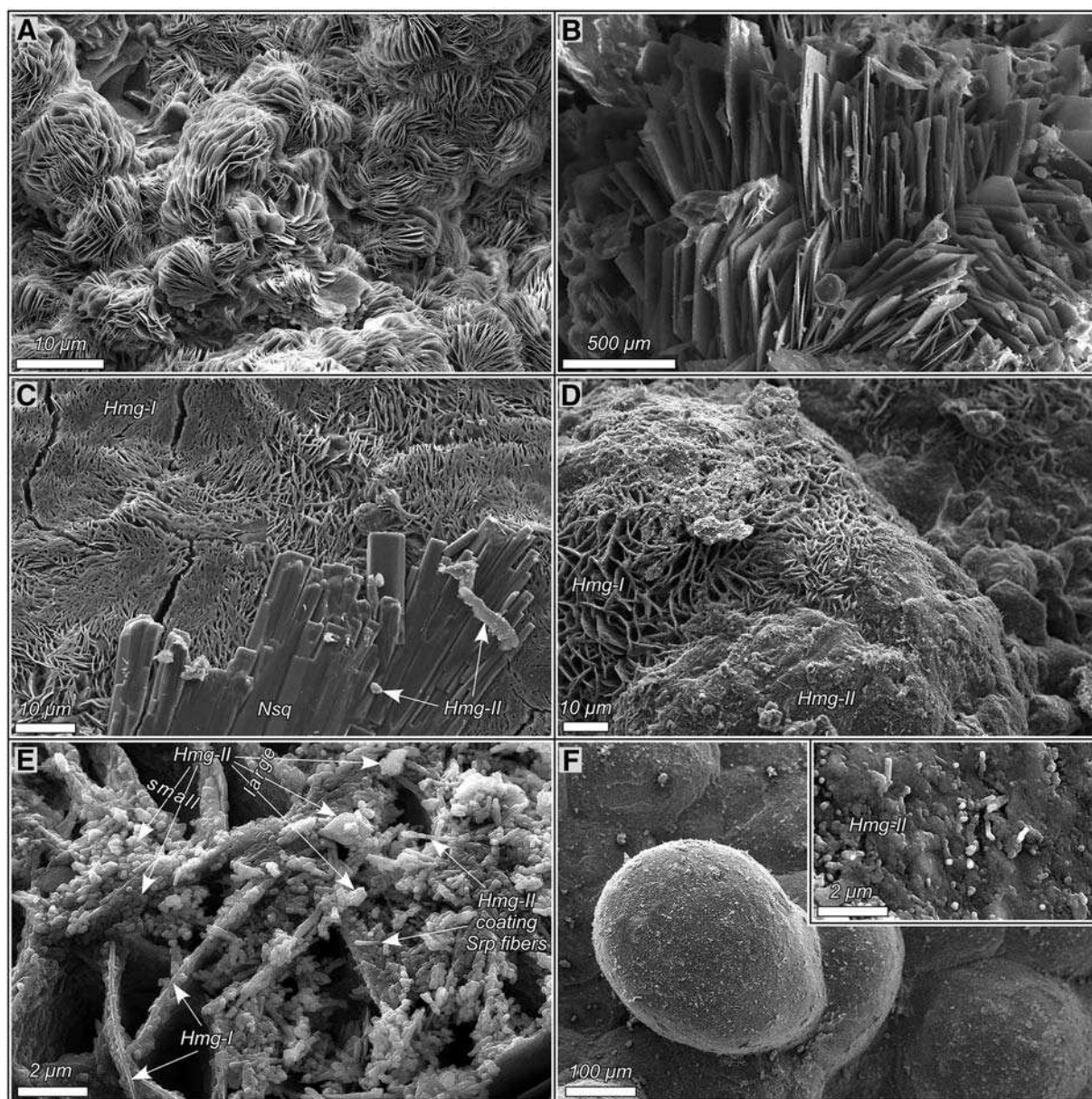


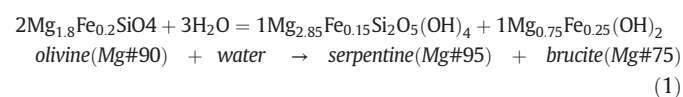
**Fig. 11.** SEM-SE photos of hydrous Mg carbonates. A) Crust and botryoidal aggregates of early Hmg made of lenticular crystals; B) Detail of an early Hmg rosette made of sharp blade crystals; C) Prismatic crystals of Nsq overgrowing a crust of early Hmg (Hmg-I); D) Early Hmg crusts (Hmg-I) coated by a very fine grained crust of late Hmg (Hmg-II); E) Detail of late Hmg (Hmg-II) coating lenticular crystals of early Hmg (Hmg-I); note the variable size of crystallites and some Srp fibres coated by Hmg; F) A rosette of early Hmg entirely coated by late Hmg; in the inset a detail of coating with crystallites merging in a continuous smooth crust. Abbreviations as in Fig. 3.

However, mechanisms of serpentinization and the reason of the formation of different final mineral assemblages are still debated (Bach et al., 2006; Beard et al., 2009; Frost and Beard, 2007; Frost et al., 2013; Klein et al., 2009, 2014). Some authors proposed that the process is mainly triggered by the chemistry of the protolith or of the incoming fluid (Bach et al., 2006; Frost et al., 2013; Schwarzenbach et al., 2016). They indicated, for example, that early-stage serpentinization starts at low W/R ratio (quasi-isochemical), with the hydration of olivine to serpentine and ferroan brucite. With increasing degree of serpentinization, alteration of pyroxene (in pyroxene-rich mantle rocks, such as harzburgites and lherzolites) produces an increase of silica activity in the fluids, dissolution of ferroan brucite and formation of magnetite (Bach et al., 2006; Frost et al., 2013). The final mineral assemblages of a fully serpentinized harzburgite are expected to be brucite-free.

Alternatively, Klein et al., 2014 report the strong influence of temperature in the process. They showed that magnetite-rich serpentinites

have Fe-poor brucite and are formed at temperatures of 200–300 °C. Magnetite-poor samples are associated with Fe-rich brucite and are formed at temperatures <200 °C.

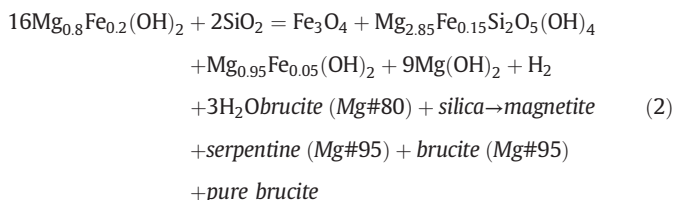
At Montecastelli, harzburgites and dunites show distinct serpentinization parageneses, suggesting a marked link between the protolith composition and the different observed mineral assemblages. The initial hydration of olivine in dunites (Type 2a) and harzburgites, led to initial formation of Fe-rich brucite, serpentine and magnetite-poor assemblages, according to the reaction (Bach et al., 2006; Eq. (R1)):



Most likely, the alteration of pyroxene in Type 1 serpentinized harzburgites, produced the  $a_{\text{SiO}_2}$  and  $a_{\text{Al}_2\text{O}_3}$  increases, and the complete dissolution of early-formed brucite, as reported elsewhere in

serpentinized harzburgites. In contrast, the oceanic serpentinization of the pyroxene-poor dunites (Type 2a) did not produce an increase in  $a_{\text{SiO}_2}$  and  $a_{\text{Al}_2\text{O}_3}$  in the fluids. Here, the process went to completion without chemical changes that could have enhanced brucite dissolution.

However, the Montecastelli serpentinized dunites record a late additional serpentinization event. Type 2b dunites show a pervasive recrystallization of the previous assemblage (Type 2a). The new assemblage, made of fine-grained magnetite, Fe-poor brucite and serpentine, likely developed at higher temperatures (>200 °C; Klein et al., 2014) and/or higher  $f\text{O}_2$ . Alternatively, it could be the result of the influx of relatively Si-rich fluid that interacted with the surrounding harzburgites (orthopyroxene-rich; Bach et al., 2006; Frost et al., 2013).  $X_{\text{Mg}}$  of the analysed serpentines does not change during the transition from 2a to 2b, even if a complete recrystallization is observed. For this reason, we did not take the contribution of ferric ion into account, which is potentially hosted in the serpentine structure (as reported in Frost et al., 2013). The reaction can be summarized as:



The assemblage serpentine–brucite–magnetite is not particularly common (Schwarzenbach et al., 2016). Frost et al. (2013) suggested that this assemblage exists on a univariant line with a negative slope

in  $f\text{O}_2$ – $\mu\text{SiO}_2$  (see Fig. 9 in Frost et al., 2013). They concluded that the transition from the divariant serpentine–Fe-rich brucite field to the univariant serpentine–Fe-poor brucite–magnetite field is consistent with an increase in the redox budget (equivalent to ferric iron content) of the rock as the time-integrated fluid–rock ratio increases.

At Montecastelli, the transition from Type 2a to Type 2b serpentinized dunite does not mark the progressive increase of water/rock ratio, as confirmed by the almost complete serpentinization already acquired by Type 2a rocks. Our data are more consistent with a veining/replacement process, triggered by the infiltration of a later and chemically distinct batch of fluids, also characterized by comparatively higher temperatures.

## 6.2. The carbonation process

The ongoing carbonation at Montecastelli is controlled by the presence of extensive amounts of both Fe-rich and Fe-poor brucite in serpentinized dunite bodies (Types 2a and 2b) and triggered by the present-day infiltration of meteoric water. Serpentinized harzburgites (Type 1), lack any carbonation effect. Minor hydromagnesite encrustation is related to the migration of water that previously reacted with nearby dunites.

Brucite is known to be a mineral that easily dissolves in water at low temperatures, four orders of magnitude faster than olivine and chrysotile (Beinlich and Austrheim, 2012; Mumpton and Thompson, 1966; Pokrovsky and Schott, 2004; Snow and Dick, 1995). Klein and Garrido (2011) reported a thermodynamic model of serpentinite carbonation indicating that brucite, when present (in serpentinized peridotites with molar olivine/orthopyroxenes ratio > 1), is always the first phase

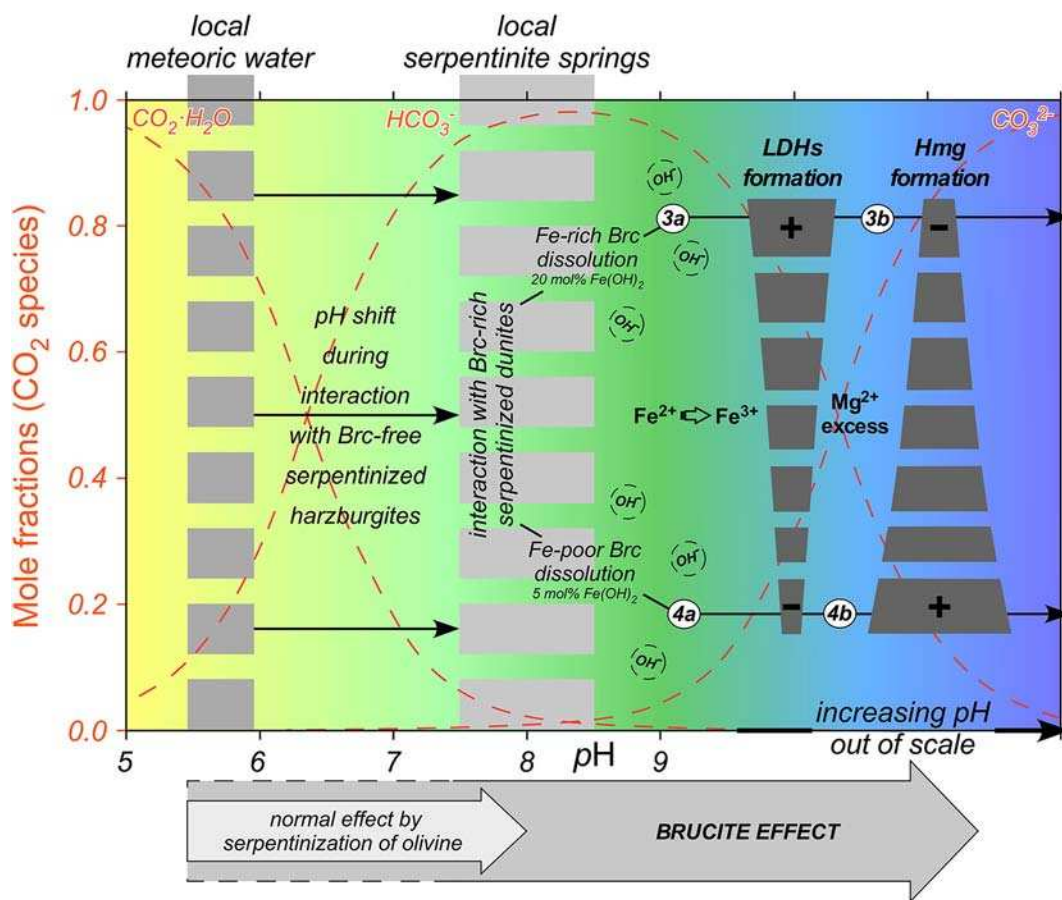


**Fig. 12.** Interpretive qualitative diagram for the water/rock interaction processes occurring at Montecastelli. The sequential interactions between meteoric water, serpentinized harzburgites and serpentinized dunites are shown together with the main dissolution/precipitation processes occurring at different pH values. The proposed sequence reflects field, petrographic and chemical data collected at Montecastelli.



reacting with dissolved carbon to form Mg-carbonates (i.e., magnesite at  $T > 100$  °C; hydrous Mg-carbonates at  $T < 80$ – $60$  °C; Hopkinson et al., 2012; Gautier et al., 2014).

The modal proportion of brucite in the serpentinites appears to be the main parameter among others (i.e., humidity; temperature; proportion of  $\text{CO}_2$  in the air; microbial activity; watering frequency; particle size) determining the maximum storage capacity of  $\text{CO}_2$  (Assima et al., 2013, 2014; Pronost et al., 2011). The Montecastelli serpentinitized dunites have a high, yet variable, modal brucite content (in the range 10–20%; from petrographic and diffractometric estimates) that is consistent with available estimates for other serpentinitized dunites worldwide (D'Antonio and Kristensen, 2004; Hyndman and Peacock, 2003).

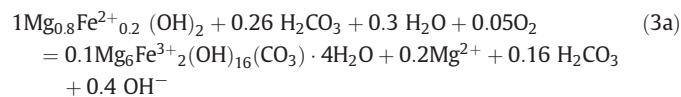
The dissolution of brucite in water is a surface-controlled reaction accelerated by the presence of organic/inorganic ligands (Pokrovsky et al., 2005). Ligands that promote brucite dissolution are those that form protonated ions at neutral to weakly alkaline pH (e.g.  $\text{HCO}_3^-$  at  $\text{pH} \approx 8.5$ ; Fig. 12). Deprotonated ions (e.g.  $\text{CO}_3^{2-}$ ) inhibit dissolution, usually enhancing carbonate precipitation (at  $\text{pH} > 9$ ).

The Montecastelli local meteoric waters (Bedini, 2016) show normal slightly acidic pH, while several spring waters discharged from serpentinitized harzburgites in our area have been significantly modified in their pH (up to  $\text{pH} = 7.5$ – $8.5$ ; Fig. 12). A significant pH increase is frequently achieved by meteoric waters flowing through serpentinitized peridotites due to the ongoing secondary weak serpentinization of the few primary silicate relicts (olivine, pyroxene; Hostetler et al., 1966). The spring water issued from serpentinitized harzburgites at the top of serpentinitized dunite hillock has a pH of 8–8.5. At this pH, the predominant carbonic species is  $\text{HCO}_3^-$  and the water has the maximum potential to dissolve brucite in serpentinitized dunites. We suggest that infiltration of slightly alkaline  $\text{HCO}_3^-$  dominated waters into the serpentinitized dunites induces brucite dissolution, and, depending on water/rock ratio, the progressive further increase of pH in solution (Fig. 12). At higher pH, the stable  $\text{CO}_3^{2-}$  enhances the observed carbonates precipitation.

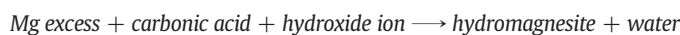
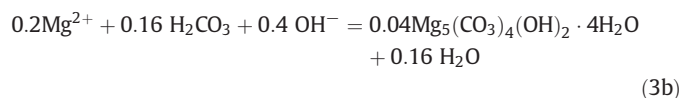
### 6.3. The brucite-effect on the mineral CCS efficiency

Petrographic and geochemical data indicate that the serpentinitized dunites containing Fe-rich brucite (Type 2a) react with fluid to produce a carbonate assemblage dominated by LDHs and minor amounts of hydromagnesite. Type 2b serpentinitized dunites, characterized by a Fe-poor brucite assemblage, produce a large amount of hydromagnesite and minor LDHs. We can balance stoichiometry and charge of two extreme reactions that are relevant for Montecastelli. Reactions were calculated considering 1 mol of brucite as a reagent and pyroaurite + hydromagnesite as solid products. Similar reactions can be calculated using coalingite + hydromagnesite as solid products.

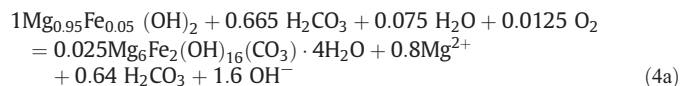
Reactions 3a–3b describe interaction between carbonic water and Type 2a Fe-rich brucite (20 mol.%  $\text{Fe}(\text{OH})_2$ ), as:



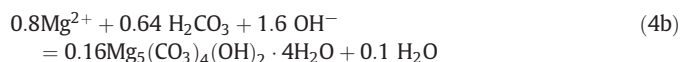
Brucite [80%  $\text{Mg}(\text{OH})_2$ ] + carbonic acid + water + oxygen  $\longrightarrow$  pyroaurite + Mg excess + carbonic acid + hydroxide ion



Reactions 4a–4b describe the interaction between carbonic water and Type 2b Fe-poor brucite (5 mol.%  $\text{Fe}(\text{OH})_2$ ), as:



Brucite [95%  $\text{Mg}(\text{OH})_2$ ] + carbonic acid + water + oxygen  $\longrightarrow$  pyroaurite + Mg excess + carbonic acid + hydroxide ion



Mg excess + carbonic acid + water + hydroxide ion  $\longrightarrow$  hydromagnesite + water

Both reactions 3a–3b and 4a–4b have been subdivided into two steps to highlight the observed sequential precipitation of LDHs and hydromagnesite. The oxidizing character of the water transforms  $\text{Fe}^{2+}$  to  $\text{Fe}^{3+}$ . The concomitant pH increase induces precipitation of LDHs (reactions 3a and 4a). At higher pH, the remaining fluid, containing variable amounts of Mg in excess, precipitates hydromagnesite (in situ and/or along the fractures and at the rock surface; reactions 3b and 4b).

Depending on the chemical composition of brucite and its Fe content, the amount of resulting pyroaurite and hydromagnesite is different (reactions 3a,b and 4a,b). If brucite is stoichiometrically identical to pyroaurite (i.e., molar  $\text{Fe}/\text{Fe} + \text{Mg} = 0.25$ ), only LDHs will precipitate. For brucite composition even higher in iron, an excess of  $\text{Fe}^{3+}$  is expected, probably resulting in extensive precipitation of hydroxides along with LDHs. The same consideration can be developed for coalingite, though considering the different stoichiometry of this mineral (molar  $\text{Fe}/\text{Fe} + \text{Mg} = 0.17$ ).

The efficiency of reactions 3a–3b and 4a–4b, in light of an optimization of mineral CCS technology, can be roughly evaluated. The net result of reaction 3a–3b is the dissolution of one mole of Fe-rich brucite (20 mol.%  $\text{Fe}(\text{OH})_2$ ) and the sequestration of 0.26 mol of  $\text{CO}_2$  by precipitation of 0.1 mol of pyroaurite and 0.04 mol of hydromagnesite. In contrast, the consumption of one mole of Fe-poor brucite (reactions 4a–4b) sequesters an amount of  $\text{CO}_2$  2.6 times larger (0.665 mol) than reaction 3a–3b, precipitating 0.025 mol of pyroaurite and 0.16 mol of hydromagnesite. The efficiency of  $\text{CO}_2$  sequestration is very different in the two cases, owing to the distinct carbon content of LDHs (ca. 1.5 wt.%) and hydromagnesite (ca. 10 wt.%).

The maximum efficiency for  $\text{CO}_2$  mineralogical sequestration is reached in the case of pure brucite. Unfortunately, most of the natural occurrences of brucite from ophiolite complexes involve Fe-rich brucite. In order to maximize the mineral CCS, a strategy is needed for inhibiting LDH formation (for example, provoking early precipitation of Fe hydroxides), and maximizing the precipitation of hydromagnesite.

## 7. Conclusions

The Montecastelli ophiolite complex represents an exceptional case study, providing insight into the key role of brucite in driving the carbonation reaction. The oceanic serpentinization of reactive dunite bodies produced the observed brucite-bearing serpentinites. The nearby spinel harzburgites were altered to brucite-free serpentinites. Their exhumation and their tectonic stacking up to the present geological setting, created the conditions for brucite-driven on-going carbonation.

The mineralogical complexity (brucite variably enriched in Fe), produced by multiple stages of oceanic serpentinization is today responsible for the different proportion of carbonates (hydromagnesite vs. LDHs). Carbonation of Fe-rich brucites produces large amounts of LDHs and less hydromagnesite. Alteration of Fe-poor brucite results in smaller amounts of LDHs. A larger excess of Mg is released that leads to an extensive precipitation of hydromagnesite inside and outside the dunite reactor zone. Hydromagnesite can trap a larger amount of carbon compared to LDHs, increasing the efficiency of CO<sub>2</sub> sequestration.

Overall, this study identifies the best rock type (and the most suitable mineral) to be used for the induced mineral CCS and for future implementations of this technology.

Supplementary data to this article can be found online at <http://dx.doi.org/10.1016/j.lithos.2017.07.005>.

## Acknowledgements

This research is partially supported by RESPIRA project (POR-FSE 2007–2013; Regione Toscana – EU) and by Pegaso PhD project (2012–2015; Regione Toscana; XVIII Cycle). CB and co-authors thank Gianluca Giorgi, the owner of the Montecastelli Mine (<https://sites.google.com/site/minieradelpavone/>) who allowed us to study the mining dump and helped us to sample fluids and rocks. A. Langone, M. Lorenzoni, C. Natali, and S. Vezzoni are thanked for helping with field sampling. M. Scambelluri, A. Bracco, J. Sadighi, E. Schwarzenbach and two anonymous reviewers are thanked for their comments that greatly improved the manuscript.

## References

- Akao, M., Marumo, F., Iwai, S., 1974. The crystal structure of hydromagnesite. *Acta Cryst B* 30, 2670.
- Aleksandrov, S.M., Senin, V.G., 2005. Genesis, composition, and evolution of sulfide mineralization in magnesian skarns. *Geochemistry International* 43 (6), 559–577.
- Anselmi, B., Mellini, M., Viti, C., 2000. Chlorine in the Elba, Monti Livornesi and Murlo serpentines: evidence for sea-water interaction. *European Journal of Mineralogy* 12, 137–146. <http://dx.doi.org/10.1127/ejm/12/1/0137>.
- Assima, G.P., Larachi, F., Beaudoin, G., Molson, J., 2013. Accurate and direct quantification of native brucite in serpentine ores – new methodology and implications for CO<sub>2</sub> sequestration by mining residues. *Thermochimica Acta* 566, 281–291. <http://dx.doi.org/10.1016/j.tca.2013.06.006>.
- Assima, G.P., Larachi, F., Molson, J., Beaudoin, G., 2014. Comparative study of five Quebec ultramafic mining residues for use in direct ambient carbon dioxide mineral sequestration. *Chemical Engineering Journal* 245, 56–64. <http://dx.doi.org/10.1016/j.cej.2014.02.010>.
- Bach, W., Garrido, C.J., Paulick, H., Harvey, J., Rosner, M., 2004. Seawater-peridotite interactions: first insights from ODP Leg 209, MAR 15°N. *Geochemistry, Geophysics, Geosystems* 5 (9). <http://dx.doi.org/10.1029/2004GC000744>.
- Bach, W., Paulick, H., Garrido, C.J., Ildefonse, B., Meurer, W.P., Humphris, S.E., 2006. Unraveling the sequence of serpentinization reactions: petrography, mineral chemistry, and petrophysics of serpentinites from MAR 15N (ODP Leg 209, Site 1274). *Geophysical Research Letters* 33 (13). <http://dx.doi.org/10.1029/2006GL025681>.
- Baronnet, A., Boudier, F., 2001. Microstructural and Microchemical Aspects of Serpentinization, Lunar and Planetary Science Conference XI, Abstract 3382.
- Bea, S.A., Wilson, S.A., Mayer, K.U., Dipple, G.M., Power, I.M., Gamazo, P., 2012. Reactive transport modelling of natural carbon sequestration in ultramafic mine tailings. *Vadose Zone Journal* 11 (2), 1–17. <http://dx.doi.org/10.2136/vzj2011.0053>.
- Beard, J.S., 2000. Occurrence and composition of tochilinite and related minerals in Site 1068 serpentinites. In: Beslier, M.-O., Whitmarsh, R.B., Wallace, P.J., Girardeau, J. (Eds.), *Proceedings ODP. Scientific Results Vol. 173*, pp. 1–9.
- Beard, J.S., Frost, B.R., Fryer, P., McCaig, A., Searle, R., Ildefonse, B., Zinin, P., Sharma, S.K., 2009. Onset and progression of serpentinization and magnetite formation in olivine-rich troctolites from IOCP Hole U1309D. *Journal of Petrology* 50, 387–403. <http://dx.doi.org/10.1093/petrology/egp004>.
- Bedini, F., 2016. Serpentinite Carbonation at Montecastelli Pisano (Tuscany, Italy): Implications for CO<sub>2</sub>-mineral Sequestration in Ultramafic Rocks. Ph.D. thesis. The University of Pisa, Italy.
- Beinlich, A., Austrheim, H., 2012. In situ sequestration of atmospheric CO<sub>2</sub> at low temperature and surface cracking of serpentinized peridotite in mine shafts. *Chemical Geology* 332–333, 32–44. <http://dx.doi.org/10.1016/j.chemgeo.2012.09.015>.
- Bertolani, M., Rivalenti, G., 1973. Le mineralizzazioni metallifere della miniera di Montecatini in Val di Cecina (Pisa). *Bollettino della Società Geologica Italiana* 92, 635–648.
- Boschi, C., Dini, A., 2015. Ultramafic-hosted copper deposits from Ligurian Ophiolites (Southern Tuscany, Italy). Workshop Mantle, Water and Life: The Ultramafic-hosted Rainbow Hydrothermal Field – Lyon 10th–12th June 2015.
- Boschi, C., Dini, A., Dallai, L., Ruggieri, G., Gianelli, G., 2009. Enhanced CO<sub>2</sub>-mineral sequestration by cyclic hydraulic fracturing and Si-rich fluid infiltration into serpentinites at Malenatura (Tuscany, Italy). *Chemical Geology* 265, 209–226. <http://dx.doi.org/10.1016/j.chemgeo.2009.03.016>.
- Boschi, C., Bonatti, E., Ligi, M., Brunelli, D., Cipriani, A., Dallai, L., D'Orazio, M., Früh-Green, G.L., Tonarini, S., Barnes, J.D., Bedini, R.M., 2013a. Serpentinization of mantle peridotites along an uplifted lithospheric section, Mid Atlantic Ridge at 11°N. *Lithos* 178, 3–23.
- Boschi, C., Dini, A., Baneschi, I., Bedini, F., Dallai, L., Perchiazzi, N., 2013b. Direct carbon dioxide uptake from the atmosphere: examples from Montecastelli serpentinites (Tuscany, Italy). *Proceeding of the ACEME 2013*. ISBN: 978-94-6018-655-4, pp. 431–441.
- D'Antonio, M., Kristensen, M.B., 2004. Serpentine and brucite of ultramafic clasts from the South Chamorro Seamount (Ocean Drilling Program Leg 195, Site 1200): inferences for the serpentinization of the Mariana forearc mantle. *Mineralogical Magazine* 68 (6), 887–904. <http://dx.doi.org/10.1180/0026461046860229>.
- Dini, A., Gianelli, G., Puxeddu, M., Ruggieri, G., 2005. Origin and evolution of Pliocene–Pleistocene granites from the Larderello geothermal field (Tuscan Magmatic Province, Italy). *Lithos* 81, 1–31. <http://dx.doi.org/10.1016/j.lithos.2004.09.002>.
- Elter, P., 1975. Tensional and compressional areas in the recent (Tortonian to present) evolution of the northern Apennines. *Bollettino di Geofisica Teorica ed Applicata* 17 (65), 3–18.
- Federici, F., 1941. *Relazione geologico mineraria sul giacimento cuprifero di Montecastelli Pisano*. Goito.
- Frost, B.R., Beard, J.S., 2007. On silica activity and serpentinization. *Journal of Petrology* 48 (7), 1351–1368. <http://dx.doi.org/10.1093/petrology/egm021>.
- Frost, B.R., Evans, K.A., Swapp, S.M., Beard, J.S., Mothersole, F.E., 2013. The process of serpentinization in dunite from New Caledonia. *Lithos* 178, 24–39. <http://dx.doi.org/10.1016/j.lithos.2013.02.002>.
- Gautier, Q., Bénéth, P., Mavromatis, V., Schott, J., 2014. Hydromagnesite solubility product and growth kinetics in aqueous solution from 25 to 75 °C. *Geochimica et Cosmochimica Acta* 138, 1–20. <http://dx.doi.org/10.1016/j.gca.2014.03.044>.
- Godard, M., Lagabrie, Y., Alard, O., Harvey, J., 2008. Geochemistry of the highly depleted peridotites drilled at ODP Sites 1272 and 1274 (Fifteen–Twenty Fracture Zone, Mid-Atlantic Ridge): implications for mantle dynamics beneath a slow spreading ridge. *Earth and Planetary Science Letters* 267, 410–425. <http://dx.doi.org/10.1016/j.epsl.2007.11.058>.
- Hänchen, M., Prigobbe, V., Baciocchi, R., Mazzotti, M., 2008. Precipitation in the Mg-carbonate system: effects of temperature and CO<sub>2</sub> pressure. *Chemical Engineering Science* 63, 1012–1028. <http://dx.doi.org/10.1016/j.ces.2007.09.052>.
- Harrison, A.L., Power, I.M., Dipple, G.M., 2013. Accelerated carbonation of brucite in mine tailings for carbon sequestration. *Environmental Science & Technology* 47, 126–134. <http://dx.doi.org/10.1021/es3012854>.
- Harrison, A.L., Dipple, G.M., Power, I.M., Mayer, K.U., 2015. Influence of surface passivation and water content on mineral reactions in unsaturated porous media: implications for brucite carbonation and CO<sub>2</sub> sequestration. *Geochimica et Cosmochimica Acta* 148, 477–495.
- Hart, S.R., Zindler, A., 1986. In search of a bulk-earth composition. *Chemical Geology* 57, 247–267.
- Hébert, R., Serri, G., Hekinian, R., 1989. Mineral chemistry of ultramafic tectonites and ultramafic to gabbroic cumulates from the major oceanic basins and Northern Apennine ophiolites (Italy) – a comparison. *Chemical Geology* 77, 183–207. [http://dx.doi.org/10.1016/0009-2541\(89\)90074-0](http://dx.doi.org/10.1016/0009-2541(89)90074-0).
- Hopkinson, L., Kristova, P., Rutt, K., Cressey, G., 2012. Phase transitions in the system MgO–CO<sub>2</sub>–H<sub>2</sub>O during CO<sub>2</sub> degassing of Mg-bearing solutions. *Geochimica et Cosmochimica Acta* 76, 1–13. <http://dx.doi.org/10.1016/j.gca.2011.10.023>.
- Hostetler, P.B., Coleman, R.G., Mumpton, F.A., Evans, B.W., 1966. Brucite in alpine serpentinites. *American Mineralogist* 51, 75–98.
- Hövelmann, J., Putnis, C.V., Ruiz-Agudo, E., Austrheim, H., 2012. Direct nanoscale observations of CO<sub>2</sub> sequestration during brucite [Mg(OH)<sub>2</sub>] dissolution. *Environmental Science & Technology* 46 (9), 5253–5260. <http://dx.doi.org/10.1021/es300403n>.
- Hyndman, R.D., Peacock, S.M., 2003. Serpentinization of the forearc mantle. *Earth and Planetary Science Letters* 212, 417–432. [http://dx.doi.org/10.1016/S0012-821X\(03\)00263-2](http://dx.doi.org/10.1016/S0012-821X(03)00263-2).
- IPCC, 2005. In: Metz, B., Davidson, O., de Coninck, H.C., Loos, M., Meyer, L.A. (Eds.), *IPCC Special Report on Carbon Dioxide Capture and Storage*. Prepared by Working Group III of the Intergovernmental Panel on Climate Change. Cambridge University Press, Cambridge, United Kingdom and New York, NY, USA 442 pp.
- IPCC, 2014. *Climate Change 2013 – The Physical Science Basis: Working Group I Contribution to the Fifth Assessment Report of the Intergovernmental Panel on Climate Change*. Cambridge University Press, Cambridge.
- Jagoutz, E., Palme, H., Baddenhausen, H., Blum, K., Cendales, M., Dreibus, G., Spettel, B., Lorenz, V., Wanke, H., 1979. The Abundances of Major, Minor and Trace Elements in the Earth's Mantle as Derived from Primitive Ultramafic Nodules. *Lunar and Planetary Science Conference Proceedings Vol. 10* pp. 2031–2050.
- Jambor, J.L., 1976. New occurrences of the hybrid sulfide tochilinite. *Geological Survey of Canada Paper* 76, 65–69.
- Jöns, N., Kahl, W.-A., Bach, W., 2017. Reaction-induced porosity and onset of low-temperature carbonation in abyssal peridotites: insights from 3D high-resolution microtomography. *Lithos* 268–271, 274–284. <http://dx.doi.org/10.1016/j.lithos.2016.11.014>.
- Klein, F., Garrido, C.J., 2011. Thermodynamic constraints on mineral carbonation of serpentinized peridotite. *Lithos* 126 (3–4), 147–160. <http://dx.doi.org/10.1016/j.lithos.2011.07.020>.
- Klein, F., Bach, W., Jöns, N., McCollom, T., Moskowitz, B., Berquó, T., 2009. Iron partitioning and hydrogen generation during serpentinization of abyssal peridotites from 15°N on the Mid-Atlantic Ridge. *Geochimica et Cosmochimica Acta* 73, 6868–6893. <http://dx.doi.org/10.1016/j.gca.2009.08.021>.



- Klein, F., Bach, W., Humphris, S.E., Kahl, W.A., Jöns, N., Moskowitz, B., Berquó, T.S., 2014. Magnetite in seafloor serpentinite—some like it hot. *Geology* 42 (2):135–138. <http://dx.doi.org/10.1130/G35068.1>.
- Langone, A., Banerchi, I., Boschi, C., Dini, A., Guidi, M., Cavallo, A., 2013. Serpentinite-water interaction and chromium (VI) release in spring waters: examples from Tuscan ophiolites. *Ophioliti* 38 (1):41–57. <http://dx.doi.org/10.4454/ofioliti.v38i1.415>.
- Loring, J.S., Thompson, C.J., Zhang, C., Wang, Z., Schaef, H.T., Rosso, K.M., 2012. In situ infrared spectroscopic study of brucite carbonation in dry to water-saturated supercritical carbon dioxide. *The Journal of Physical Chemistry* 116:4768–4777. [dx.doi.org/10.1021/jp210020t](http://dx.doi.org/10.1021/jp210020t).
- Lotti, B., 1885. Sul giacimento cuprifero di Montecastelli Pisano. *Bollettino del Reale Comitato geologico d'Italia XVI*, Roma.
- Lotti, B., 1924. Rapporto sulla miniera cuprifera di Montecastelli in Toscana. Rapporto interno Montecatini. Società Generale per l'Industria Mineraria e Chimica :pp. 1–14. <http://www.neogeo.unisi.it/dbgmnew/ricerca.asp?act=see&id=12922>.
- Marroni, M., Pandolfi, L., 1996. The deformation history of an accreted ophiolite sequence: the Internal Liguride Unit (Northern Apennines, Italy). *Geodinamica Acta* 9:13–29. <http://dx.doi.org/10.1080/09853111.1996.11417260>.
- Mellini, M., Rumori, C., Viti, C., 2005. Hydrothermally reset magmatic spinels in retrograde serpentinites: formation of “ferritchromit” rims and chlorite aureoles. *Contributions to Mineralogy and Petrology* 149:266–275. <http://dx.doi.org/10.1007/s00410-005-0654-y>.
- Mills, S.J., Christy, A.G., Genin, J.M.R., Kameda, T., Colombo, F., 2012. Nomenclature of the hydrotalcite supergroup: natural layered double hydroxides. *Mineralogical Magazine* 76 (5), 1289–1336.
- Moll, M., Paulick, H., Suhr, G., Bach, W., 2007. Data report: microprobe analyses of primary phases (olivine, pyroxene, and spinel) and alteration products (serpentine, iowaite, talc, magnetite, and sulfides) in Holes 1268A, 1272A, and 1274A. In: Kelemen, P.B., Kikawa, E., Miller, D.J. (Eds.), *Proceedings ODP, Scientific Results 209: College Station, TX (Ocean Drilling Program)*:pp. 1–13 <http://dx.doi.org/10.2973/odp.proc.sr.209.003.2007>.
- Mumpton, F.A., Thompson, C.S., 1966. The stability of brucite in the weathering zone of the new Idria serpentinite. *Clays and Clay Minerals* 14 (1):249–257. <http://dx.doi.org/10.1346/CCMN.1966.0140122>.
- Nirta, G., Pandeli, E., Principi, G., Bertini, G., Cipriani, N., 2005. The Ligurian units of Southern Tuscany. *Bollettino della Società Geologica Italiana* 3, 29–54.
- Niu, Y., 2004. Bulk-rock major and trace element compositions of abyssal peridotites: implications for mantle melting, melt extraction and post-melting processes beneath mid-ocean ridges. *Journal of Petrology* 45 (12), 2423–2458.
- Organova, N.I., Gorshkov, A.I., Dikov, Yu.P., Kul'bachinskiya, V.A., Laputina, I.P., Sivtsov, A.V., Sluzhenikin, S.F., Ponomarenko, A.I., 1988. New data on tochilinite. *International Geology Review* 30 (6):671–705. <http://dx.doi.org/10.1080/00206818809466050>.
- Oskierski, H.C., Dlugogorski, B.Z., Jacobsen, G., 2013. Sequestration of atmospheric CO<sub>2</sub> in chrysotile mine tailings of the Woodsreef Asbestos Mine, Australia: quantitative mineralogy, isotopic fingerprinting and carbonation rates. *Chemical Geology* 358: 156–169. <http://dx.doi.org/10.1016/j.chemgeo.2013.09.001>.
- Pokrovsky, O.S., Schott, J., 2004. Experimental study of brucite dissolution and precipitation in aqueous solutions: surface speciation and chemical affinity control. *Geochimica et Cosmochimica Acta* 68:31–45. [http://dx.doi.org/10.1016/S0016-7037\(03\)00238-2](http://dx.doi.org/10.1016/S0016-7037(03)00238-2).
- Pokrovsky, O.S., Schott, J., Castillo, A., 2005. Kinetics of brucite dissolution at 25 °C in the presence of organic and inorganic ligands and divalent metals. *Geochimica et Cosmochimica Acta* 69 (4):905–918. <http://dx.doi.org/10.1016/j.gca.2004.08.011>.
- Pronost, J., Beaudoin, G., Tremblay, J., Larachi, F., Duchesne, J., Hebert, R., Constantin, M., 2011. Carbon sequestration kinetic and storage capacity of ultramafic mining waste. *Environmental Science & Technology* 45:9413–9420. <http://dx.doi.org/10.1021/es203063a>.
- Rumori, C., Mellini, M., Viti, C., 2004. Oriented, non-topotactic olivine → serpentine replacement in mesh-textured, serpentinitized peridotites. *European Journal of Mineralogy* 16:731–741. <http://dx.doi.org/10.1127/0935-1221/2004/0016-0731>.
- Schwarzenbach, E.M., Caddick, M.J., Beard, J.S., Bodnar, R., 2016. Contributions to Mineralogy and Petrology 171 (5). <http://dx.doi.org/10.1007/s00410-015-1219-3>.
- Serri, G., Hébert, R., Hékinian, R., 1985. Chemistry of ultramafic tectonites and ultramafic to gabbroic cumulates from the major oceanic basins and the Northern Apennines ophiolites. *Ophioliti* 10, 63–76.
- Snow, J.E., Dick, H.J.B., 1995. Pervasive magnesium loss by weathering of peridotite. *Geochimica et Cosmochimica Acta* 59:4219–4235. [http://dx.doi.org/10.1016/0016-7037\(95\)00239-V](http://dx.doi.org/10.1016/0016-7037(95)00239-V).
- Tribuzio, R., Thirlwall, M.F., Vannucci, R., 2004. Origin of the gabbro–peridotite association from the northern Apennine Ophiolites (Italy). *Journal of Petrology* 45 (6):1109–1124. <http://dx.doi.org/10.1093/petrology/egh006>.
- Viti, C., Mellini, M., Rumori, C., 2005. Exsolution and hydration of pyroxenes from partially-serpentinized harzburgites. *Mineralogical Magazine* 69, 491–500.
- Wicks, F.J., Whittaker, E.J.W., 1977. Serpentine textures and serpentinization. *Canadian Mineralogist* 15, 459–488.
- Wilson, S.A., Dipple, G.M., Power, I.M., Thom, J.M., Anderson, R.G., Raudsepp, M., Gabites, J.E., Southam, G., 2009. Carbon dioxide fixation within mine wastes of ultramafic-hosted ore deposits: examples from the Clinton Creek and Cassiar Chrysotile Deposits, Canada. *Economic Geology* 104:95–112. <http://dx.doi.org/10.2113/gsecongeo.104.1.95>.
- Wilson, S.A., Dipple, G.M., Power, I.M., Barker, S.L.L., Fallon, S.J., Southam, G., 2011. Subarctic weathering of mineral wastes provides a sink for atmospheric CO<sub>2</sub>. *Environmental Science & Technology* 45:7727–7736. <http://dx.doi.org/10.1021/es202112y>.
- Wilson, S.A., Harrison, A.L., Dipple, G.M., Power, I.M., Barker, S.L.L., Ulrich Mayer, K., Fallon, S.J., Raudsepp, M., Southam, G., 2014. Offsetting of CO<sub>2</sub> emissions by air capture in mine tailings at the Mount Keith Nickel Mine, Western Australia: rates, controls and prospects for carbon neutral mining. *International Journal of Greenhouse Gas Control* 25:121–140. <http://dx.doi.org/10.1016/j.ijggc.2014.04.002>.
- Zarandi, A.E., Larachi, F., Beaudoin, G., Plante, B., Sciortino, M., 2016. Multivariate study of the dynamics of CO<sub>2</sub> reaction with brucite-rich ultramafic mine tailings. *Int. J. Green. Gas Contr.* 52:110–119. <http://dx.doi.org/10.1016/j.ijggc.2016.06.022>.
- Zhao, L., Sang, L., Chen, J., Ji, J., Teng, H.H., 2010. Aqueous carbonation of natural brucite: relevance to CO<sub>2</sub> sequestration. *Environmental Science & Technology* 44 (1): 406–411. <http://dx.doi.org/10.1021/es9017656>.